STELLAR MASS PROFILES OF GALAXIES IN THE HUBBLE FRONTIER FIELDS: EVIDENCE FOR MASS DEPENDENCY IN ENVIRONMENTAL QUENCHING

Vivian Yun Yan Tan

A THESIS SUBMITTED TO
THE FACULTY OF GRADUATE STUDIES
IN PARTIAL FULFILLMENT OF THE REQUIREMENTS
FOR THE DEGREE OF

MASTER OF SCIENCE

Graduate Program in Physics and Astronomy
York University, Toronto, Ontario

July 2020

Abstract

In this thesis, we analyze the mass profiles of cluster and field galaxies from the Hubble Frontier Fields at redshifts of $0.25 < z < 0.6$ to explore the effect environment has on the stellar mass distribution of star-forming and quiescent galaxies. We seek to explain how the two main types of quenching (mass and environment) affect the morphology of quiescent galaxies, and whether environmental and mass quenching are truly separable. The deep, high resolution photometry of the Frontier Fields were utilized to create resolved stellar mass maps, that were parametrically fit to 2D Sersic profiles in order to obtain the mass profiles. Overall, mass profile Sersic indices (n_{mass}) tend to be higher than the H-band light profile Sersic indices, although only the n_{mass} of field galaxies is shown to be significantly different from the n_{light} of the H-band Sersic profiles, with a p-value of their similarity at 0.0063. The effective radius R_{mass} is on the whole, quite similar between mass and H-band light profiles for both cluster and field galaxies.

The quiescent cluster sample was separated into two morphological groups of disk-like and bulge-like using the distribution of Sersic parameters of the star-forming galaxies' mass profiles. Quiescent cluster galaxies that have both their n_{mass} and R_{mass} within 2σ of the respective mean parameter for the star-forming galaxies were placed into the disk-like category. 44% of the quiescent cluster galaxy sample is considered disk-like, with over 74% of these galaxies falling into this category at the lowest masses, which is in the $10^{8} M_{\odot}$ to $10^{9.5} M_{\odot}$ range. This indicates most disk-like quiescents in clusters, which are most likely environmentally quenched, are low mass satellite galaxies, with "satellite" meaning any galaxy that is not the brightest cluster galaxy in a cluster. The slope of the environmental quenching efficiency ϵ_{ρ} versus stellar mass for the two quiescent morphological groups are both non-zero, with disk-like quiescents having an overall slope of -0.19, and bulge-like quiescents

having a positive slope of 0.36. This shows environmental quenching is stellar mass dependent, and affects galaxies with $M_\star < 10^{9.5} M_\odot$ more than galaxies above that mass limit.

Acknowledgements

I would like to thank my supervisor, Prof. Adam Muzzin for his impeccable guidance and advice, as well as the other members of our research group both current and former, Visal Sok, Dr. Cemile Marsan, Dr. Leo Alcorn, and Dr. Jasleen Matharu. The Hubble Frontier Fields data is provided to us by Prof. Danilo Marchesini of Tufts University, and was created by Prof. Heath Shipley of Tufts University. Finally, I would like to thank the Department of Physics and Astronomy at York University for supporting my research.

-Vivian Tan

Date 2019

Table of Contents

List of Tables

List of Figures

Chapter 1

Introduction

1.1 The diversity of galaxies

Large scale surveys, such as the SDSS (York et al., 2000), have shown that galaxies in the local universe, i.e. at $z = 0$, can be classified into two main groups: star-forming and quiescent. When plotted in a colour-magnitude diagram, they fall into a bimodal distribution: they either have blue or red colours, with very few in between (Balogh et al., 2004b; Brinchmann et al., 2004; Baldry et al., 2006; Salim et al., 2007). If a galaxy has blue colours, it is actively forming stars, because young stars dominate the blue and UV parts of the spectrum. Galaxies with red colours usually have low star-formation rates and older stellar populations, although they may be actively star-forming but red due to dust extinction. It seems that red-sequence galaxies are found in much higher numbers in dense regions of the universe, such as galaxy clusters (Kauffmann et al., 2004; Balogh et al., 2004a; Baldry et al., 2006; Smith et al., 2006; van den Bosch et al., 2008; Peng et al., 2010). They are also on average more massive than star-forming galaxies as well (Baldry et al., 2006; Bamford et al., 2009; Graves et al., 2009; Cooper et al., 2010; Peng et al., 2010).

Apart from large ellipticals at the center of clusters, galaxies seem to be morphologically distinct in the local universe, and can be clearly delineated into the S/S0/E groupings of the Hubble sequence (Hubble, 1926), where S indicates spiral galaxies, E denoting ellipticals, and S0s are in-between elliptical and spiral, and contain both a disk and a prominent bulge. In the Hubble scheme, both Es and S0s are also called "early type" while spirals are called "late types". In this thesis, we simply describe any galaxy that is bulge dominated as bulge-like, which includes ellipticals and most S0s, and any galaxy with a small or non-existent bulge are called disk-like. Most star-forming galaxies are disk-like, and a large number of quiescent galaxies are bulge-like, though the bulge size varies. Surveys of the local and distant universe have also shown that galaxies residing in denser environments tend to be bulge-like (i.e. "early type") rather than disk-like (Oemler, 1974; Davis & Geller, 1976; Postman & Geller, 1984; Bamford et al., 2009). This is the well known morphology-density relation as described by Dressler (1980).

Galaxies almost always begin on the blue sequence, with the exception of dusty/high-metallicity star-forming galaxies, and will eventually turn off star-formation and migrate to the red-sequence (see the review by Blanton & Moustakas, 2009). This transition is usually also accompanied by a morphological change from a disk galaxy to an elliptical galaxy, or at least bulge growth in the central regions. Migrating from blue to red can occur slowly through the gradual depletion of their reservoir of cold gas, or quickly (on a timescale $t <<1$ Gyr) by consuming the gas in a violent starburst, or losing the gas through internal or external interactions (Bell et al., 2012; Wetzel et al., 2012). The latter we will refer to as "quenching" in this thesis. The peak of cosmic star formation was at $z \sim 2$ when most galaxies were blue and star-forming, so the proportion of star-forming galaxies to quiescent galaxies must increase from low redshift ($z \sim 0$) to $z \sim 2$. There is evidence that the fraction of bulge-like galaxies in clusters decreases between $z \sim 0$ and $z \sim 1$ (van Dokkum et al., 2000; Lubin et al., 2002; Postman et al., 2005). In addition, Cerulo et al. (2017) found that most of the bulge-like cluster galaxies which were quenched between $z \sim 1$ to today seem to be S0s, not ellipticals . Clusters are always evolving, and the environment of a cluster would be different at $z \sim 1$ compared to the present day. Determining whether a galaxy had become quiescent because of its internal processes, or because of the influences of its environment is one of the most important questions in galaxy evolution.

1.2 Mass and environment as drivers of galaxy quenching

There are many quenching mechanisms - processes that quickly and drastically reduce the star formation rate to zero or almost zero, which depend on interactions with other galaxies. The quenching processes involved may be tidal stripping (Merritt, 1984), tidal harassment/heating (Moore et al., 1996), or starvation (Larson et al., 1980). This is why dense environments like a cluster contain more quiescent galaxies than the field, and continue to grow their fraction of quiescents at a higher rate. A galaxy cluster also contains hot diffuse gas called the intracluster medium, and this wind from the ICM can strip cold gas from galaxies when they fall into the gravitational potential of the cluster (Gunn & Gott, 1972). If quenching happens because of the effects of the environment surrounding the galaxy, then that is defined as environmental quenching. Tidal interactions and ram pressure stripping are obvious examples. If a galaxy quenches due to internal processes, such as AGN feedback or supernovae feedback, this is considered self quenching, also called mass quenching (Peng et al., 2010), since this type of quenching tends to have a higher occurrence in more massive galaxies. The lines between environmental and self-quenching may not be quite so distinct, since it has been shown that tidal interactions and mergers drive AGN feedback (Ellison et al., 2008, 2011; Bluck et al., 2020).

Some of the first studies using observational data show the effects of mass and environment on quenching are completely separable and independent in the local universe, and possibly up to $z \sim 1$ (Peng et al., 2010; Muzzin et al., 2012; Quadri et al., 2012; Kovač et al., 2014). The idea is simply to assume mass quenching operates at the same efficiency across all environmental densities, i.e. there are some galaxies that by a quirk of their nature will quench themselves without any interactions with its surroundings. Environmental quenching only increases in frequency in proportion to the environmental density (which is the number density of galaxies in a certain volume of space), and does not depend on other factors, such as the stellar mass of the galaxy. This seems to hold for the local universe, but more recent studies that focus on redshifts in the range of $z \sim 0.5$ to $z \sim 1$, and beyond, find more evidence that environmental quenching does not solely depend on environmental density, but also on the stellar mass of the galaxy (Balogh et al., 2016; Darvish et al., 2016; Kawinwanichakij et al., 2017; Lin et al., 2017; Pintos-Castro et al., 2019).

Red-sequence galaxies have been observed to have more diversity in morphology (see review by Blanton & Moustakas, 2009), and this may arise from the diverse ways galaxies can quench. Perhaps the connection between environmental quenching and stellar mass is that different quenching methods occur with more frequency at certain stellar masses.

Our method for making the connection between main-sequence star-forming and red-sequence galaxies is by examining stellar mass distributions of galaxies. Assuming that in most cases of quenching, stellar mass is conserved within the galaxy (which means ignoring quenching by mergers), then star-forming galaxies at a certain mass must have quenched into quiescent galaxies of the same mass. Assuming stellar mass conservation as a galaxy evolves is appropriate for most quenching scenarios; for ram-pressure stripping, starvation, or feedback, the cold gas is removed on such quick time scales that the stellar mass of the galaxy stays stagnant as it quenches (Dekel & Silk, 1986; Abadi et al., 1999; Veilleux et al., 2005).

1.3 Stellar mass mapping

A common method of studying the structure or morphology of galaxies is through its integrated light profile. Usually a Sersic function is used to model the light distribution of the galaxy, due to the versatility of its parameters to describe a large number of galaxy types. For example, a low Sersic index ($n \sim 1$) correlates to Hubble's classification of late-type galaxies, while a higher Sersic index, ($n \gtrsim 4$) correlates to Hubble's classification of early-type galaxies. There are several studies that examined morphology via mass distribution by using colour gradients as a proxy for mass to measure the half-mass radii (Szomoru et al., 2013), as well as mass-to-light ratios (van der Wel et al., 2014; Suess et al., 2019). Generally when integrated light profiles are used, only light in one band is used. Both colour gradients and integrated light profiles may not truly reflect the underlying stellar mass distribution;

without the full spectral energy distribution, the stellar mass of a galaxy can only be approximated. In order to know how much stellar mass is contained in a galaxy, the spectral energy distribution (SED) must be measured. The SED of a galaxy is simply the superposition of the spectra of every single star within it. Using what we know about the mass-luminosity relationship of each type of star, the stellar mass content of a galaxy can be determined from its spectra. Information about the gas and dust content of a galaxy can be obtained from its SED as well, and it can help distinguish between a red galaxy that is dusty but star-forming and one that is quiescent.

When only photometry is available, there are ways of estimating a stellar mass for a galaxy without complete spectral information. Recently there have been works that use the method of SED-fitting, which takes the existing photometry of a galaxy at certain wavelengths, and according to a selected stellar population synthesis model, along with a library of existing stellar SEDs, fits a spectral energy distribution that best approximates of the underlying stellar mass content. Elmegreen et al. (2007) and Förster Schreiber et al. (2011) pioneered this method for $z \sim 1.4$ and $z \sim 2$ galaxies respectively with NICMOS data. This technique is however highly dependent on signal-to-noise, which means it is excellent for *integrated* stellar mass but pixel-by-pixel SED-fitting is not as reliable. Even resolved studies must rely on pixel-binning to maximize the signal-to-noise since that increases the accuracy of the SED output. Since high-redshift galaxies cannot be as resolved as ones at $z = 0$, resolved SED-fitting for the high-redshift universe was limited to studies of large structures of galaxies that contain a substantial amount of signal-to-noise, such as star-forming clumps in Förster Schreiber et al. (2011) and Wuyts et al. (2012), or tidal tails in Elmegreen et al. (2007). Nevertheless, despite the limitations, Wuyts et al. (2012) utilized this method to discover that many bright UV clumps had no more stellar mass than the less bright disk of these galaxies. These studies demonstrate the feasibility of using resolved SED-fitting for morphological studies of distant galaxies. Recently, there are deeper surveys at intermediate redshift, such as the Hubble Frontier Fields, which make it possible to construct resolved stellar mass maps from which bulge size or half-mass radius may be obtained. Mapping the stellar mass content of cluster and field galaxies between $z \sim 0$ and $z \sim 1$ might bring new insights into the morphological changes that galaxies undergo during the environmental quenching process.

1.4 Motivation and Outline

The approach we take to more closely study the relationship between morphology and environmental quenching is to find a population of cluster satellite and field galaxies that are at an intermediate redshift of $0 < z < 1$. A catalog that has deep multiband photometry of both cluster and field environments is the Hubble Frontier Fields (Shipley et al., 2018). The six clusters that were observed for this catalog all have redshifts between $0.3 < z < 0.6$. The details of this catalog are described in Chapter 2. The stellar mass distribution of these galaxies will be obtained and studied. When quenching occurs, the underlying stellar mass distribution of galaxies is unlikely to change substantially, unless mergers are involved. In clusters, mergers mainly occur between satellites and the brightest cluster galaxy (BCG), with satellites referring to any galaxy that does not dominate the gravitational potential of the cluster. BCGs can increase their mass two or threefold via mergers (Lidman et al., 2012; Lin et al., 2013; Bellstedt et al., 2016). However, those satellites are lost, and satellite-satellite mergers are much rarer in clusters because the relative velocities of satellites with respect to each other are very high, making the cross-section for interactions unlikely.

For stellar mass map creation, the method that is used in Wuyts et al. (2012) will be applied. Their process involves pixel-binning of images via Voronoi tesselation to maximize signal-to-noise, and then applying SED-fitting for the integrated flux of each bin. There are other ways to obtain stellar mass maps, such as using rest-frame $u - g$ colours (Szomoru et al., 2013). However, since we have resolved HST photometry, we can use a more intensive stellar population fitting method. For galaxy modelling, we use the latest version of the GALFIT code (Peng et al., 2002) to fit 2D Sersic profiles onto the resolved stellar mass maps. This is also expanded on in chapter 3. As opposed to using the flux distribution of galaxies and making inferences about mass distribution, mapping the underlying stellar mass of galaxies is the most direct way to study galaxy morphology. By fitting 2D Sersic profiles to the stellar mass maps instead of integrated light, we can more directly probe the morphology of the underlying stellar mass and quantify it with Sersic parameters. Throughout this thesis, we adopt a ΛCDM cosmology with $H_0 = 70$km s^{-1}, $\Omega_m = 0.3$, and $\Omega_\Lambda = 0.7$.

Chapter 2

Data Sample

We utilized the Hubble Frontier Fields catalog (HFF, release paper Shipley et al., 2018) for this analysis. The catalog contains six lensing clusters and six flanking fields taken with the UVIS, ACS, and WFC3 cameras on the Hubble Space telescope. Additional imaging is also provided in this catalog from both space and ground-based observatories such as VLT/HAWK-I, Keck/MOSFIRE, and Spitzer/IRAC. The region of the sky which the Frontier Fields focuses on contains many lensed background galaxies, which is why their HST data has such depth, and why a diverse selection of instruments were also used for the creation of this catalog (Lotz et al., 2017). More detail on the HFF catalogs is provided in §2.1 along with which observations we used or did not use and justifications for why. The images of the clusters and the field are taken parallel to each other, at the same time, but with different cameras; When Hubble images the cluster with ACS, it images the "flanking field" with WFC3, and vice versa. The flanking fields will provide us with a sample of galaxies that are in less dense environments. The field images, labeled with suffix "-par", tend to have fewer bands used for imaging, as seen in table 2.1. The table B.1 in the appendix also has more information about where each filter is sourced. We refer the reader to Shipley et al. (2018) for complete details on the catalog construction process. Details on how our galaxy sample was selected is explained in section §2.2.

2.1 Summary of Catalog

For this study, we need deep high resolution photometry in order to create detailed stellar mass maps. This is why only the HST-based data is used because of the more limited spatial resolution from ground-based imaging. The native pixel resolution for WFC3/UVIS is 0.04"pixel^{-1}, for ACS is 0.049" pixel^{-1}, and for WFC3/IR is 0.128" pixel^{-1}. At the redshift range of $0.25 < z < 0.6$, this translates to 3.91-6.68 kpc arcsec^{-1} for the IR. So at the worst resolution, one HST pixel still gives us 0.855 kpc pixel^{-1}, which is sub-kpc resolution[1]. For comparison with the ground-based imaging, HAWK-I on the VLT was used to obtain observations in the Ks band, and its native pixel resolution is 0.106". But because of the effects of seeing, the best resolution from HAWK-I observations have FWHM $\sim$ 0.23" in the Ks band, and under average conditions, its seeing is $\sim$ 0.8" for an airmass of 1.2[2]. The average seeing for the Frontier Fields in the K-band is $\sim$ 0.4" (Brammer et al., 2016). This means HAWK-I observations would not have sub-kpc resolution. The IRAC observations are from 3.6-4.5 microns, and the size of the PSF is $\sim$ 0.24". Both of these instruments would not be useful for our purposes of creating resolved stellar mass maps with sub-kpc structure. It is sufficient to perform our analysis solely using the HST science images of the Frontier Fields catalogs. These are the HST observations convolved to the resolution of the $F160W$(H_{160} band), with the brightest cluster galaxies (BCGs) modelled out.

BCGs are the most massive central ellipticals in a cluster, and have masses up to $M_\star \sim 10^{12} M_\odot$. However, the Frontier Fields catalog has a more liberal definition of BCG, where any galaxy with highly extended flux in the IR filters that affects the photometry of background sources is considered a BCG. They are not as concerned with objects that may be extended in non-IR filters. The massive galaxies they chose to model out tend to be central ellipticals, however some "non-BCG" objects such as

[1]This is calculated based on the resolution of HST IR imaging from the paper by Brammer et al. (2016), as well as using the assumed cosmology stated in §1.4

[2]See Kissler-Patig et al. (2008) for more details on HAWK-I's seeing

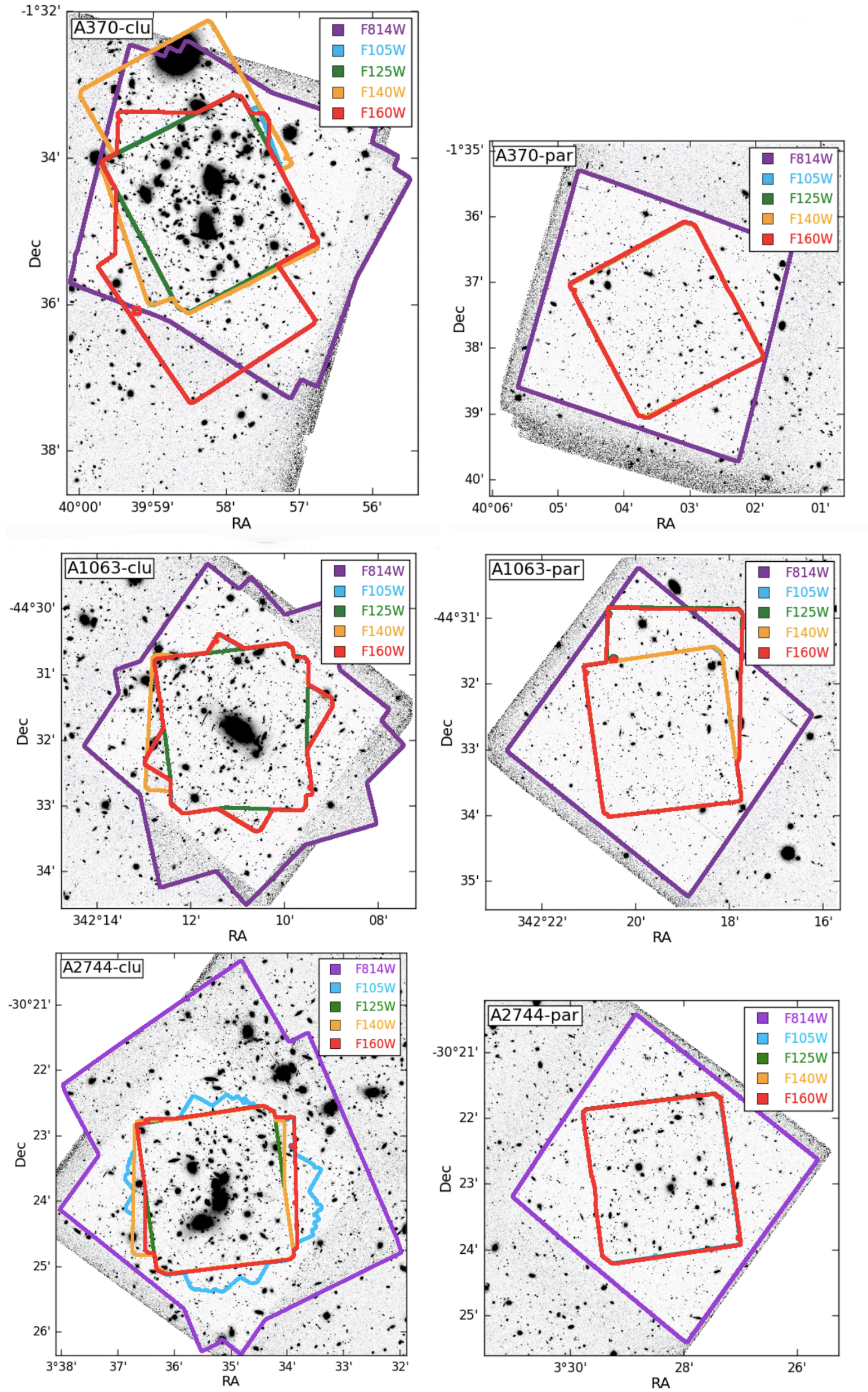

Figure (2.1) Cluster (left column) and flanking fields (right column) of Abell370, Abell1063, and Abell2744. Plots taken from Shipley et al. (2018), and shows the geometry and overlaying of five of the filters. The background image is from the F814W filter, taken by ACS on HST.

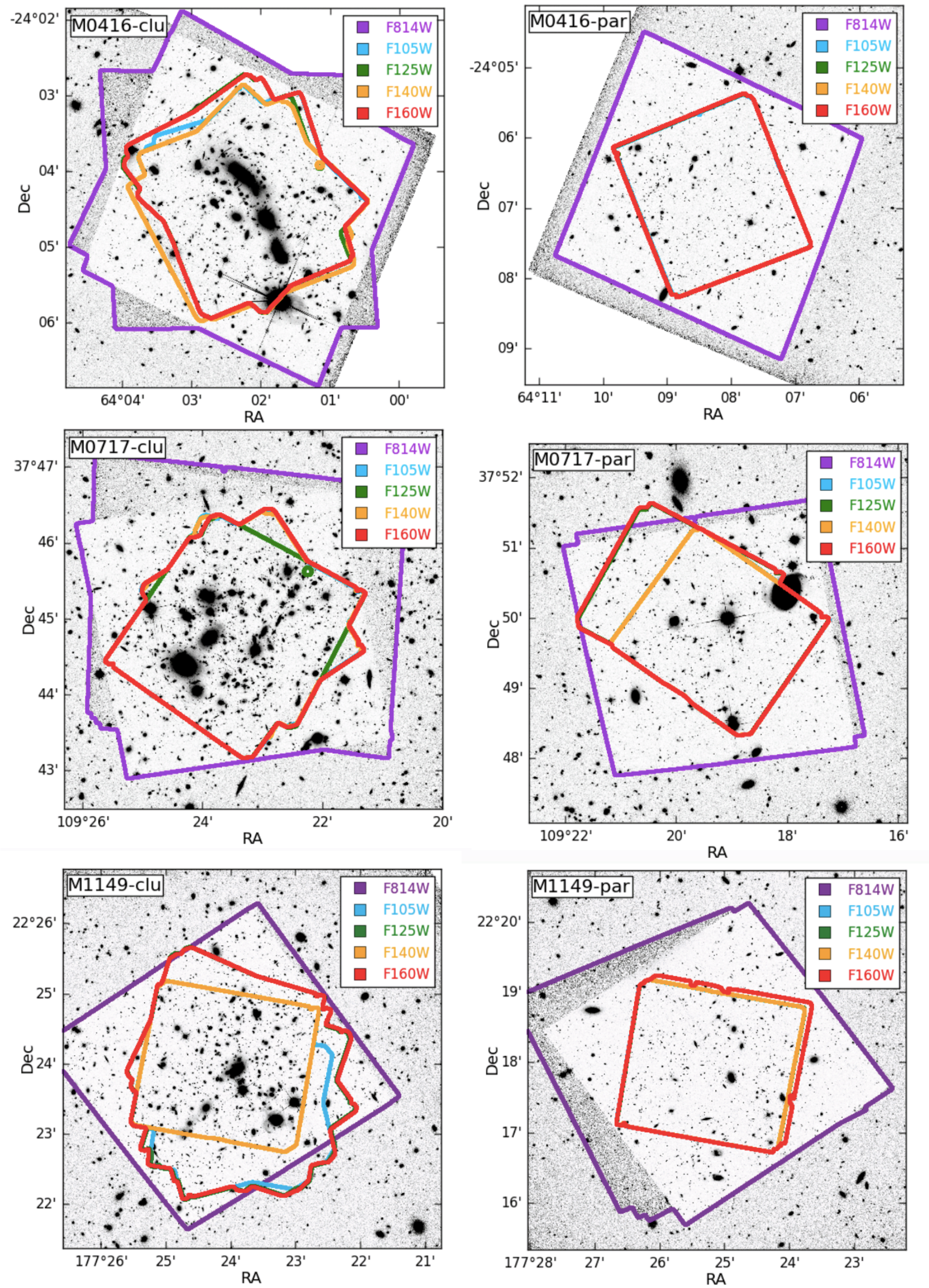

Figure (2.2) Similar to Figure 2.1 for MACS0416, MACS0717, and MACS1149.

spiral galaxies with masses of $10^{10.5}M_{\odot} - 10^{11}M_{\odot}$, can also be considered a BCG. This means that in Figures 2.1 and 2.2, nearly all of the bright galaxies that are close to the center of the cluster, not just true BCGs, would have been modelled out. This results in many "BCGs" per cluster, instead of only one true brightest cluster galaxy. Removing BCGs from the science images in the preparation of the catalog is so the flux of BCGs do not interfere with the flux of fainter galaxies (see Shipley et al., 2018 for more details). The Frontier Fields are also used to observe gravitationally lensed arcs of high redshift galaxies found in the images of the six clusters. These arcs can be more accurately studied with minimal interference of light from foreground galaxies, of which BCGs contribute the most. This thesis mainly focuses on galaxies that are at the redshifts of the clusters, but since smaller galaxies are fainter, sources down to masses of $10^{8}M_{\odot}$ can be imaged more precisely without the presence of the BCGs. The lack of more massive galaxies in the cluster sample does not affect our results. Our sample covers a mass range of $10^{8}M_{\odot} \lesssim M_{\star} < 10^{11}M_{\odot}$, while the majority of the removed massive galaxies are at masses of $10^{11}M_{\odot} \lesssim M_{\star} \lesssim 10^{12}M_{\odot}$.

Figures 2.1 and 2.2 display the six clusters and fields that make up the HFF catalog, which is taken from the Hubble Frontier Fields catalog paper (Shipley et al., 2018). Although the HFF catalogs uses up to 17 filters across all three cameras, not every cluster was imaged with all the available filters. Each cluster and field catalog has roughly 5000-8000 objects. They identify and model out the BCGs using their isophotal parameters, based on a method of modelling BCG isophotes in Ferrarese et al. (2006). They used an extremely high threshold for background subtraction in Source Extractor (abbreviated as SExtractor) (Bertin & Arnouts, 1996) to determine which galaxies are BCGs [3]. SExtractor is used again for detecting objects for the main catalogs, and this information is stored in the segmentation maps, which assigns the same number to all pixels that belong to one object, with the background set to a value of zero. The object IDs in the catalogs is their assigned numbers from the SExtractor segmentation maps.

[3]see §3.1 of Shipley et al. (2018) for more details on BCG modelling for the Frontier Fields' clusters

Table (2.1) *HST bands and sample sizes for each catalog.*

Catalog Name	Filters Used	Number of objects	Objects used
Abell370-clu Filters: 12	F275W, F336W, F435W, F475W, F606W, F625W, F814W,F105W, F110W, F125W,F140W, F160W	6795	60
Abell1063-clu Filters: 16	F225W, F275W, F336W, F390W, F435W, F475W, F606W, F625W, F775W, F814W, F850LP, F105W, F110W, F125W, F140W, F160W	7611	9
Abell2744-clu Filters: 9	F275W, F336W F435W, F606W, F814W, F105W, F125W, F140W, F160W	9390	80
MACS0416-clu Filters: 16	F225W,F275W, F336W, F390W F435W,F475W, F606W, F625W, F775W, F814W, F850LP, F105W, F110W, F125W, F140W, F160W	7431	14
MACS0717-clu Filters: 17	F225W, F275W, F336W, F390W, F435W, F475W, F555W, F606W, F625W, F775W, F814W, F850LP F105W, F110W, F125W, F140W, F160W	6370	27
MACS1149-clu Filters: 17	F225W, F275W, F336W, F390W, F435W, F475W, F555W, F606W, F625W, F775W, F814W, F850LP F105W, F110W, F125W, F140W, F160W	6868	53
Abell370-par Filters: 7	F435W, F606W, F814W F105W, F125W, F140W, F160W	5687	35
Abell1063-par Filters: 7	F435W, F606W, F814W F105W, F125W, F140W, F160W	5574	12
Abell2744-par Filters: 7	F435W, F606W, F814W F105W, F125W, F140W, F160W	6240	37
MACS0416-par Filters: 11	F435W, F475W, F606W, F625W, F775W, F814W, F850LP, F105W, F125W, F140W, F160W	7771	22
MACS0717-par Filters: 7	F435W, F606W, F814W F105W, F125W, F140W, F160W	5776	18
MACS1149-par Filters: 7	F435W, F606W, F814W F105W, F125W, F140W, F160W	5802	17

2.2 Selection of galaxies

Selection of galaxies for our sample is done on the science images provided by the Frontier Fields team. The science images were created by PSF-matching every HST observed band to the resolution of the H-band (F160W) filter, after the BCGs were modelled out of every band. They created a detection image by combining the

F814W, F105W, F125W, F140W, and F160W science images for each cluster and flanking field, and then running Source Extractor on the combined detection image. The resolution is 0.128”pixel^{-1}, which is sub-kpc resolution per pixel for our redshift range of $0.25 < z < 0.6$. The parameters used with Source Extractor are as follows: the detection and analysis thresholds are in the range of 3 - 6σ depending on the field's noise profile, the minimum area is 4 pixels for detection, the de-blending threshold is 32, and minimum contrast is 5×10^{-6}. The images were smoothed with a Gaussian filter of 4 pixels before detection. They also masked out regions that contain or are affected by bright stars, residuals of BCGs, satellite trails, and cosmic rays.

2.2.1 Cluster sample

The catalog file for each field contains the photometry in each available band, the spectroscopic redshift for any galaxies that are spectroscopically confirmed (under `z_spec`), the photometric redshift estimates (under `z_phot`) that were calculated with the program EAZY (Brammer et al., 2008), the unresolved stellar mass obtained with SED fitting through FAST (Kriek et al., 2009), as well as flags for any objects that could be problematic due to detection issues. Figure 2.3 displays all of the galaxies that were selected to be in the cluster sample as light blue circles. Any objects flagged according to the catalog are removed, and displayed in Figure 2.3 as other symbols.

After the removal of flagged objects, only the galaxies that are within ± 0.05 of the cluster's redshift are selected. In Figure 2.3, these limits are marked with the dashed blue lines that represent $z_{cluster} \pm 0.05$. For the cluster, only the objects with spectroscopically confirmed redshifts are included. This is because for the objects that have both a z_{phot} and a z_{spec}, 17% of these objects have a percent difference that is $> 20\%$ between the two redshifts. In addition, 44% of these objects have z_{phot} measurements that are more than 0.05 off from their z_{spec} measurements. This means photometric redshifts are not precise enough to determine which objects are cluster members. The objects with stellar mass $< 10^8 M_\odot$ are removed (green squares in Figures 2.3 and 2.4). Even at a stellar mass of $10^8 M_\odot$, galaxies can have an effective radius of 0.5kpc, so anything less massive than that would be unresolved.

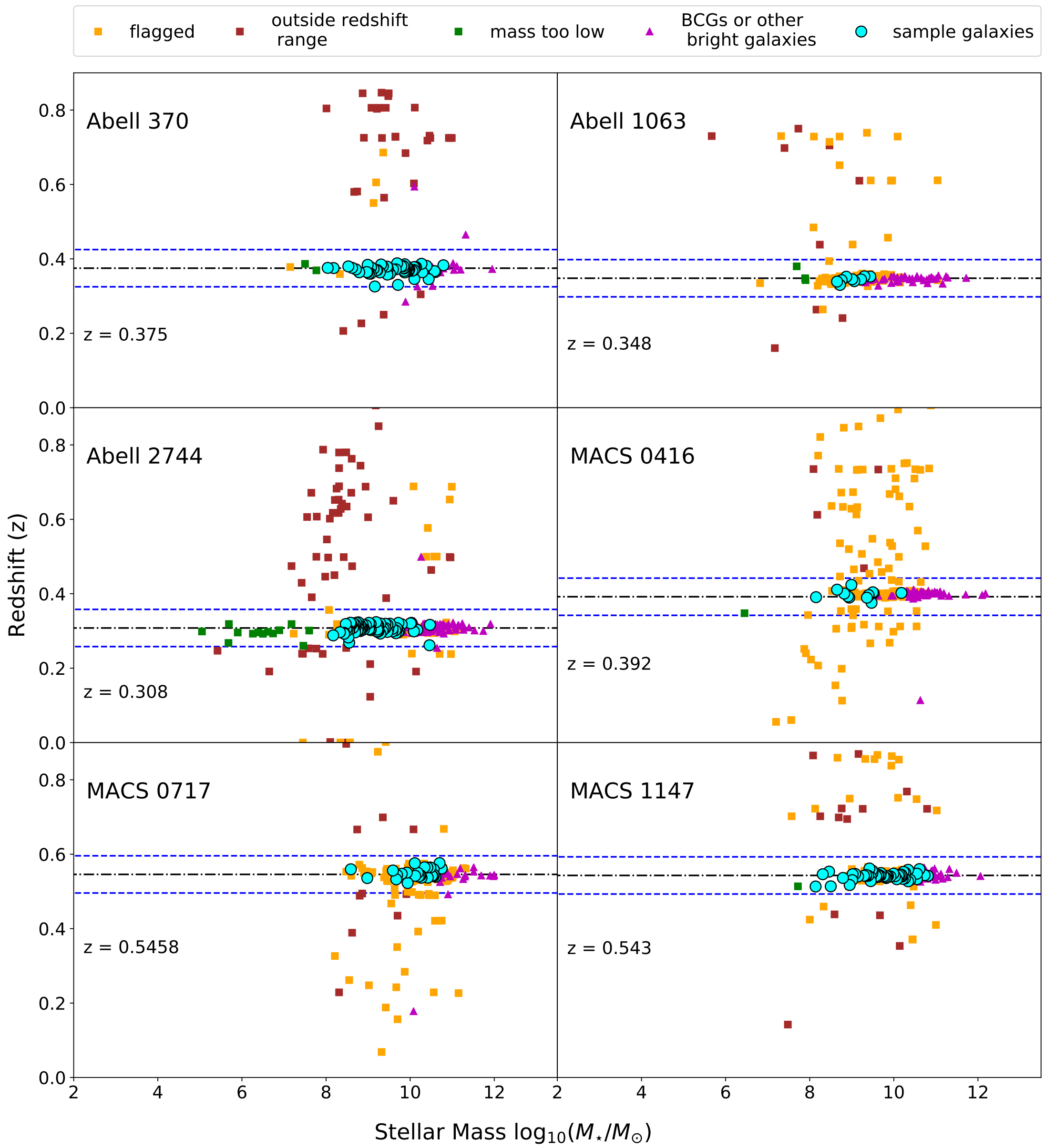

Figure (2.3) Plots showing redshift vs stellar mass demonstrating how the cluster sample of galaxies was selected. Black dashed line shows where cluster redshift is, and blue dashed lines show $z_{cluster} \pm 0.05$ redshift range where the cluster sample galaxies will be selected from. Only objects with spectroscopic redshifts are plotted, which is 3-5% of the entire catalog. "Flagged" objects are ones where their aperture is overlapping a masked region, or they have any bad flux/error/weight value (i.e. negative, NaN/Inf) for pixels associated with a source in the segmentation map.

2.2.2 Field sample

For the field sample, precise redshifts are not a necessary requirement for selection of galaxies like in the cluster sample, selecting based on photometric redshifts is sufficient. The flanking/parallel fields also do not have many objects with spectroscopically confirmed redshifts, to the point that if only selecting by z_{spec} were to occur, the sample size would be too small for proper statistical analysis (only around 60 galaxies in total). We substituted the photometric redshift for any objects that do not have spectroscopic redshifts. The redshift range chosen for selecting the field sample is $0.25 \leq z \leq 0.6$. However, the galaxies within a cluster's selection range are excluded because the flanking fields are not far enough away to be outside the cluster's virial radius. This ensures the flanking field sample is comprised of galaxies completely unaffected by the gravitational influence of a cluster.

Figure 2.4 is a redshift vs stellar mass plot similar to Figure 2.3, but it does not show all of the unselected objects due to size of the catalog. 10% of the full catalog's unselected objects are plotted in the Figure. The selected objects are however, displayed in their entirety. As mentioned in 2.1, certain galaxies in the parallel field images were also flagged as BCGs according to size or because their light profiles affected a number of nearby galaxies. The non-cluster galaxy sample has only half the number of galaxies with stellar mass $> 10^{9.5} M_{\odot}$ compared to the cluster sample. But every Frontier Fields science image has the BCGs subtracted, so there is no way of recovering those galaxies into our sample.

Cutout images of each galaxy were taken in each available band for the cluster with the dimensions of the postage stamp being around 15 to 20 times the half-light radius listed in the catalog. Similar sized cutouts of the segmentation map were made as well for the purposes of distinguishing object and background pixels. In total, there are 243 selected cluster galaxies and 141 selected field galaxies.

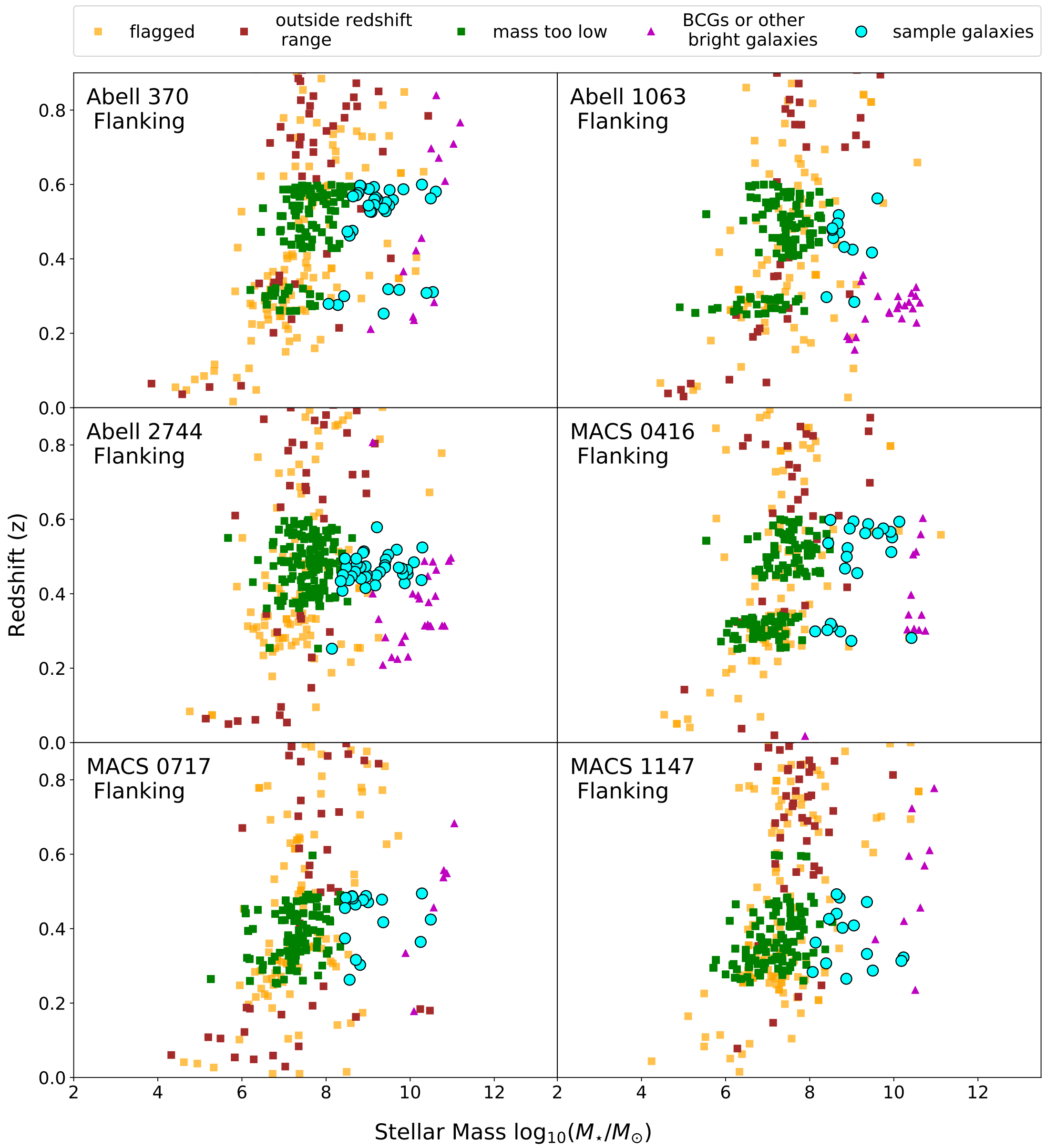

Figure (2.4) Plots showing redshift vs stellar mass demonstrating how the field sample of galaxies was selected. Selected galaxies are indicated by the light blue circles. Flagged objects follow the same rules as applied to the cluster sample. z_{phot} values are plotted when the object has no z_{spec} value.

Chapter 3

Methods

In this chapter, we present our methods for producing resolved stellar mass maps of the selected galaxy sample, and the single-component 2D Sersic profiles derived from the stellar mass. Constructing a stellar mass map is the most direct way to see how stars are distributed in a galaxy. This makes them useful for comparing star-forming to quiescent galaxies of similar stellar mass. When galaxies evolve off the star-forming main sequence and become quiescent, assuming the quenching is not due to a merger, stellar mass is usually conserved. This is because quenching means no more gas is available to be turned into stars, so the mass of stars is effectively "frozen". Morphology for galaxies can be arbitrary and subjective, but for this study, since stellar mass distributions can also be modelled by Sersic profiles, the parameters of the Sersic models of stellar mass can serve as a way of quantifying morphology.

§3.1 explains SED fitting and how the stellar mass distributions of each galaxy are created. §3.1.1 outlines making the postage stamp cutouts of equal size for the galaxy sample in every available HST band, and the binning method used to group the pixels in each image for optimal signal-to-noise. §3.2 describes single component Sersic fitting to the stellar mass maps using the galaxy modelling code GALFIT.

3.1 Resolved SED-fitting

A galaxy's stellar mass is obtained from its spectral energy distribution (SED) because it is the combined spectra of every star within that galaxy. The SED of a galaxy informs its mass-to-light ratio (M/L), which changes as the galaxy evolves, since older stellar populations are less luminous and output more in the IR than in the UV. High-quality spectra are not always available, especially for higher redshifts as is the case for our sample of galaxies, so stellar mass can also be obtained by fitting SEDs of various stellar populations to photometry in the absence of measured spectra. Most of the work on SED-fitting of distant galaxies is from ground-based observations, which means the galaxies do not have enough resolution for detailed spatial analysis of the stellar mass, and only the total unresolved stellar mass of the entire galaxy can be studied. With HFF data, we have enough resolution to map the stellar mass distribution in two spatial dimensions with multiband data. The fit will be more accurate the more photometric bands are used, and as mentioned in the previous chapter, there are 7-14 HST bands utilized for photometry. Despite good signal-to-noise for foreground pixels (these are pixels that contain flux from the selected galaxy), the background pixels remain noisy. If SED-fitting was performed pixel by pixel, the SED and measured stellar mass would be highly uncertain, especially for the outskirts of galaxies, or galaxies that have lower surface brightness. Pixel binning can fix this problem by creating bins with similar signal-to-noise ratios. The papers by Wuyts et al. (2012), Lang et al. (2014), and Chan et al. (2016) all describe various methods of stellar mass map construction by SED-fitting to photometry.

3.1.1 Pixel binning for maximizing signal-to-noise in galaxy subregions

This work uses the Voronoi binning technique created by Cappellari & Copin (2003), which was also utilized in Wuyts et al. (2012). Voronoi tessellation is most effective when modelling galaxies that have a large range in signal to noise (S/N) per pixel. This binning method creates spatial bins of equal S/N in order to best homogenize the wide range in S/N galaxies usually have, as galaxies are bright in the center and faint on the outskirts. This is why it was used in Wuyts et al. (2012), because although they were studying $z > 1$ galaxies, they were clumpy UV-bright galaxies from the CANDELS GOODS-S deep field. The HFF catalog has the same

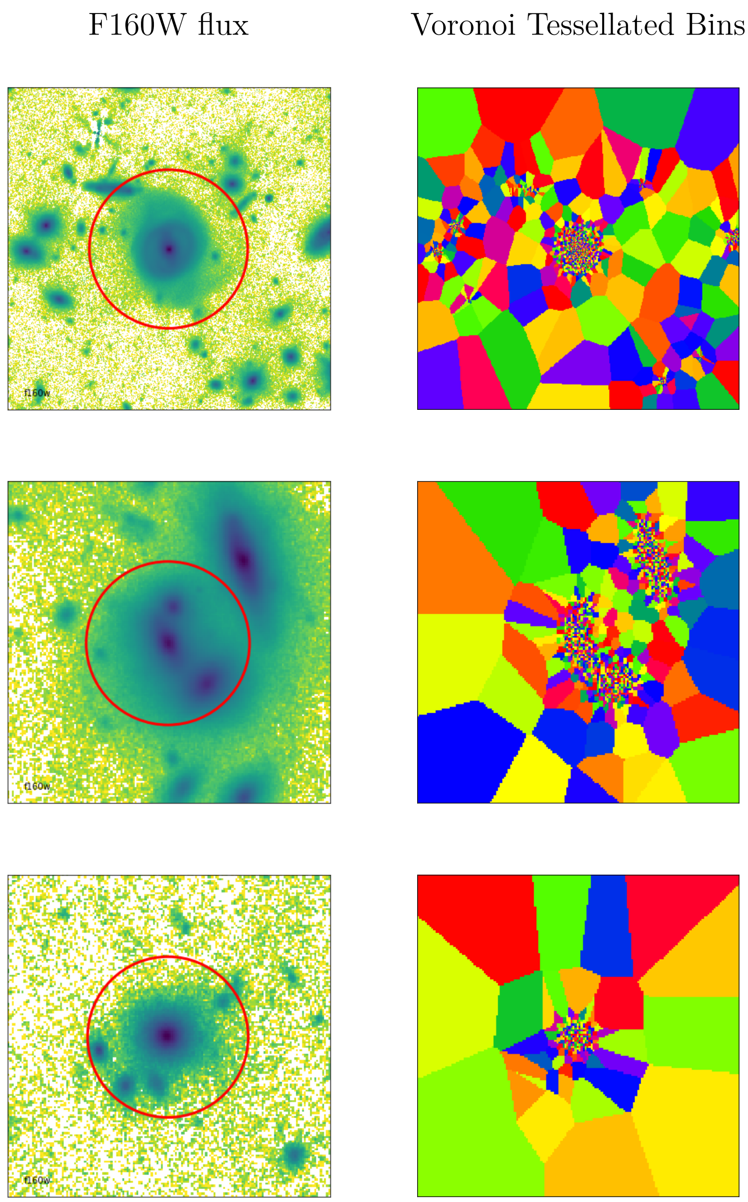

Figure (3.1) Examples of pixel binning using the weighted Voronoi tessellation algorithm from Cappellari & Copin (2003). F160W flux, which is the H-band, is the basis for the binning since IR flux correlates well to stellar mass distributions. The red circle denotes 5 times the effective radius of each galaxy.

spatial resolution as CANDELS but is deeper, so Voronoi binning is suitable for our galaxies. Cappellari & Copin (2003) designed two algorithms, weighted Voronoi tessellation (WVT) and centroid Voronoi tessellation (CVT), which work in tandem to create bins that are as circular as possible by minimizing the distances between each centroid. However, the WVT was not designed to work well with images that contain a large background with low S/N. It compensated for the low flux bins' lack of signal by adding unconnected high S/N pixels from inside the galaxy, which would result in rings of pixels from inner regions of galaxies getting added onto background bins. Only using CVT alone fixes this issue, although this results in sharper bins. This is not problematic for the images, as despite their greater resolution in comparison to previous deep Hubble surveys, their resolution is still not high enough for sharp bins to significantly affect loss of detail. Since only one filter can be used to determine bin placement, the algorithm constructed the bins based on the F160W photometry.

For most galaxies, the minimum S/N for a single bin depends on the flux of the background pixels in relation to the foreground pixels. Galaxies with less flux also tend to have a smaller angular size. The number of bins are checked against the size of the image to ensure that they have a minimum of 100 spatial bins before SED-fitting. If the flux in the target galaxy's pixels is high, the S/N for each bin will increase accordingly, though the S/N for each bin will not exceed a value of 30. The lower limit for most galaxies with low flux in the F160W filter is a S/N of 10, although for certain low surface brightness galaxies, the binning would fail unless the S/N for each bin was set to 5. What particular S/N is selected for a certain image also depends on the size of the image in relation to the number of bins. In Figure 3.1 there are three examples of how the pixel binning algorithm generates a bin map. Generally, smaller cutouts will have smaller upper and lower limits. Pixel binning will result in edges of bins leaving a residual on the resolution, and the effects of those edges means there must be a lower limit for the number of bins in an image. A scaling relation to recover resolution is applied that smooths out some of the effects of bin edges, and it will be described in §3.1.3.

Once pixel binning has finished and every galaxy has the total flux of each of its bins in every band catalogued in a data table, this catalog becomes the input for the

SED-fitting code known as FAST (Fitting and Assessment of Synthetic Templates, Kriek et al., 2009), which is one of the standard SED-fitting codes available for use.

3.1.2 Brief description of FAST

FAST is an IDL-based code for fitting stellar population synthesis models (SPS) to broadband photometry with an extensive library of template SEDs in order to study the stellar makeup of galaxies without or with incomplete spectra. Stellar population synthesis is a method where star formation histories (SFH) are assigned and used to predict which template spectra to apply accordingly. The template libraries contain SEDs of various stellar populations, especially stars off the main sequence. Other parameters that determine the fit is a given range of dust, redshifts, timescales (τ), metallicities, and star formation rates (SFRs). FAST has two SPS model choices Bruzual & Charlot, 2003 (abbreviated to BC03) and Maraston, 2005 (abbreviated to M05), and three IMFs (Salpeter, 1955; Kroupa, 2001; Chabrier, 2003).

3.1.3 Constructing the stellar mass map

To set up FAST, BC03 for stellar population synthesis was used. BC03 is one of the first comprehensive SPS codes that are used to study spectral evolution of galaxies over a span of ages, and it combines observed galaxy spectral libraries with synthetic libraries. Every simple stellar population is built with a particular initial mass function (IMF) - a function that describes the hypothetical initial population of stars in a galaxy. The SFH is the function that explains how the observed stellar population evolved from the IMF. Since BC03 was used, the IMF used must be Salpeter or Chabrier. This work uses Chabrier, as a Salpeter IMF is only applicable for cases where the dynamical mass is dominated by massive and highly luminous stars. That situation is only found in the inner regions of massive ellipticals, which are not in our sample. Chabrier has a low-mass end slope-change around 0.1 $M_{\odot}$, which means it has less low-mass stars relative to high-mass stars compared to Salpeter. A Calzetti dust law (Calzetti et al., 2000) is selected. Although Calzetti et al. (2000) used a sample of local starburst galaxies to construct the dust law, at higher redshifts,

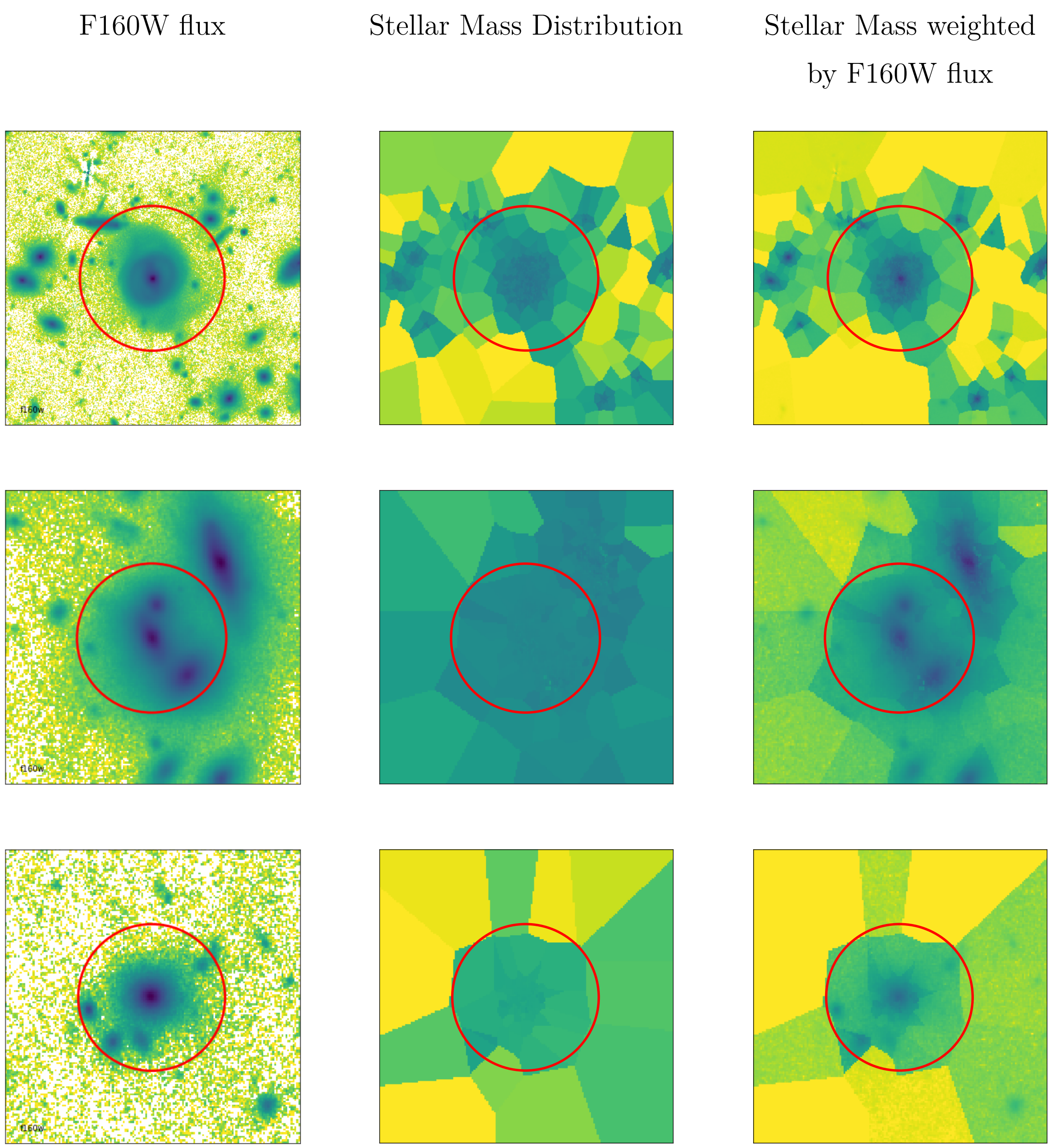

Figure (3.2) Scaling the pixels in each bin helps recover some resolution. The red circle is 5 times the effective radius of each galaxy. Note the difference between the raw stellar mass outputs from FAST in the middle column and the pixel flux-weighted stellar mass maps in the right column. The weighting is described in equation 3.2.

all galaxies would be forming stars at a higher rate than the current mean rate of star formation. Even though the mass-metallicity relation was not found to change with z, at higher redshifts, galaxies were on the whole less massive than at $z = 0$ (Mannucci et al., 2010; Stott et al., 2014). This results in metallicity decreasing as redshift increases. This means both the MW and LMC dust law would be too metal rich, and the SFR of the MW is only $2M_{\odot}$ yr^{-1}, which is too low. While this would affect some of the derived quantities, dust only has a weak effect on the M/L ratio, so the FAST-derived stellar masses are still reasonable. Recently there have been attempts to derive a dust law for higher redshifts (see Kriek & Conroy, 2013), but for the purposes of this analysis, a Calzetti dust law can still be applied without affecting the output SEDs. Both star-forming and quiescent galaxies use this dust law since dust attenuation is subdominant to other effects, and one dust law is used for simplicity

FAST is then set to fit for medium/broadband filters, for HST photometry. Every bin in a galaxy's catalog will use the same spectroscopic or photometric redshift as the galaxy itself, depending on whether z_{spec} is available for that particular galaxy. Redshifts are not free to be estimated by FAST and will be fixed according to the catalog's redshifts. The margin of error between using z_{spec} or z_{phot} with FAST is negligible in this redshift range (Muzzin et al., 2009). A tau model for SFH is adapted, which is a parameterization where star formation rate is a function of time given by the equation

$$\mathrm{SFR}(t) \sim e^{-t/\tau} \quad , \tag{3.1}$$

where τ is a free parameter. This results in log(SFR) exponentially declining over time, with τ describing how fast it declines. The limits of integration for τ, and any other parameters were all set to their maximum limits (which is from $log(\tau) = 6.5$ to $log(\tau) = 11$) so that hitting the bounds of integration does not affect the computation of the stellar mass in the final output. FAST creates an output file that contains the stellar mass of each entry in units of $\log(M_{\odot})$. A stellar mass map at the resolution of the spatial bins can be generated by assigning the bins in the image the stellar mass calculated by FAST divided by the number of pixels in the bin. In order to recover more resolution, an extra step to this process is applied, where the percent flux contribution of each pixel to the overall flux of the bin is accounted for. This scaling can also be described in an equation as

$$M_{\text{pix},i} = \left(\frac{1}{M_{bin}}\right) \frac{F_{160}^{\text{pix},j}}{\sum_{\text{bin}}^{\text{pix},j} F_{160}^{\text{pix}}} \quad , \tag{3.2}$$

where M_{bin} is the mass FAST derived for the bin, $M_{\text{pix},i}$ is the mass assigned to an individual pixel belonging to that bin, $F_{160}^{\text{pix},j}$ is the flux in the F160W band of that individual pixel, and the sum in the denominator is the total flux of the the entire bin. Figure 3.2 demonstrates the difference that scaling by contributed flux makes to

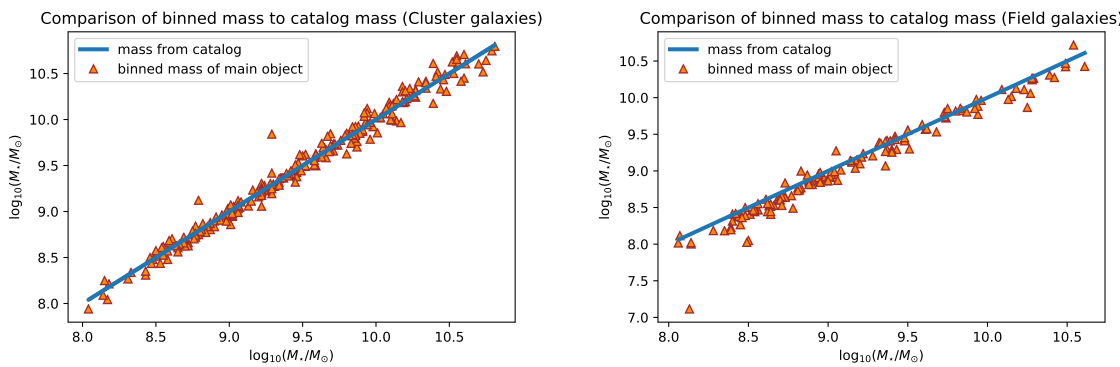

Figure (3.3) Plots comparing the unresolved stellar mass from the catalog and the total resolved stellar mass. The unresolved stellar mass (solid blue line) was obtained via SED-fitting the total flux of the object in each band, while the resolved stellar mass (orange triangles) was obtained from SED-fitting each pixel bin from the Voronoi tesselated map of the galaxy.

the bin map. The middle column shows the stellar mass without scaling by percent flux contribution, and the right column is after the scaling. There is significantly more information recovered for these maps that is obscured by only using tessellated bins. The central regions of galaxies gain more structure, and while the boundary between object and background is still obscured by the bins' boundaries, there is at least better distinction between which bins have more foreground or background pixels, especially in more crowded images such as the second row of Figure 3.2. The F160W flux is closely correlated to stellar mass at these redshifts, so this percent scaling is reasonable, and gets the mass map closer to the actual distribution of stellar mass with angular resolution consistent with the unbinned F160W HST images.

The result of creating these resolved stellar mass maps is that in principle, the accuracy of the total stellar mass for each galaxy should be improved by resolved fitting (at the Voronoi bin level), as opposed to integrated fitting over the entire galaxy. In Figure 3.3, the unresolved total stellar mass of each object is compared with the resolved total stellar mass obtained with our methods. The unresolved stellar mass from the HFF catalog was also derived with FAST, but each galaxy has only one spatial bin for FAST to fit, hence it is the unresolved mass. Note that although the two masses almost have a one-to-one relation, the resolved total mass is on average a factor of 0.03 dex lower. Sorba & Sawicki (2015) found similar results in their work on stellar mass from SED-fitting for the local universe with SDSS data.

3.2 A Sersic model of a mass profile

In order to investigate properties that are associated with the morphology of these galaxies, there must be a quantitative model that is flexible enough to accurately describe or even map certain general features of many types of galaxies. For a galaxy's light, its surface brightness distribution can be described by a Sersic profile, commonly defined as

$$I(R) = I_e \exp\left\{-b_n\left[\left(\frac{R}{R_e}\right)^{1/n} - 1\right]\right\} \quad . \tag{3.3}$$

This is a function describing how intensity or brightness I changes with respect to radius from the center of the source, R. The two main parameters that are associated with morphology is the Sersic index n, and the effective radius/half-light radius R_e (the parameter b_n can be approximated as a function of n, $b_n \sim 2n - 1/3$). When $n = 1$, the Sersic profile is an exponential profile, which describes a completely disk dominated galaxy where its flux falls off exponentially a a function of radius. When $n = 4$, this is the equivalent of a de Vaucouleurs profile, which is a bulge-dominated galaxy. Relating back to the classic Hubble classification scheme, a galaxy with a Sersic profile of $n \geq 4$ is considered an elliptical galaxy.

A Sersic profile can be used to describe a stellar mass distribution in the same way, if surface mass density as a function of radius can be analogous to intensity in equation 3.3. The following sections will describe the way stellar mass is modelled with a Sersic profile, and comparisons are made between the Sersic index from the flux-based profile with the Sersic index from the mass-based profile, as well as the difference in the half-light radius versus the half-mass radius.

3.2.1 Galaxy modelling with GALFIT

The Sersic index and effective radius for each galaxy's F160W flux density and stellar mass distribution is obtained using GALFIT (Peng et al., 2002). GALFIT is a flexible code that can fit a variety of 2D analytic functions for approximating different types of galactic structures, and takes inclination angle into account in the fit. It is also able to fit multiple functions simultaneously, making it useful for multi-component fits to a single galaxy, or fitting multiple galaxies in a single image. If galaxies in the image have a small angular separation, GALFIT may need to fit all of them to converge on a solution. The program uses a Levenberg-Marquardt minimization algorithm to find the best fits for any given image. GALFIT provides robust parametric fits to galaxy light profiles provided background estimation is done carefully. This is why the postage stamp cutouts of the selected sample in every HST band were made with the dimensions of the cutout being 20 times the half-light radius of the galaxy, so as much of the galaxy's light, or in this case, stellar mass, can be captured and compared to the background "flux". The half-light radius, or effective radius of an object is the radius that defines a circle that encompasses half the total flux emitted from the object. The half-light radii is included in the catalog and found using Source Extractor (Bertin & Arnouts, 1996), which uses the Kron radius (Kron, 1980) to define which pixels in the image to include as the total magnitude, and then defines the half-light radius from that parameter.

For each object's F160W cutout image and its stellar mass distribution, one Sersic profile is used for fitting. Spiral arms and other structures are outside the scope of this thesis because the primary goal is determining whether a galaxy is more disk-like or bulge-like. The main object being fit in each cutout is highlighted by a blue star in Figure 3.4. Since GALFIT was created for fitting surface brightness profiles, many of the parameters in the parameter file reflect this, such as one of the parameters for

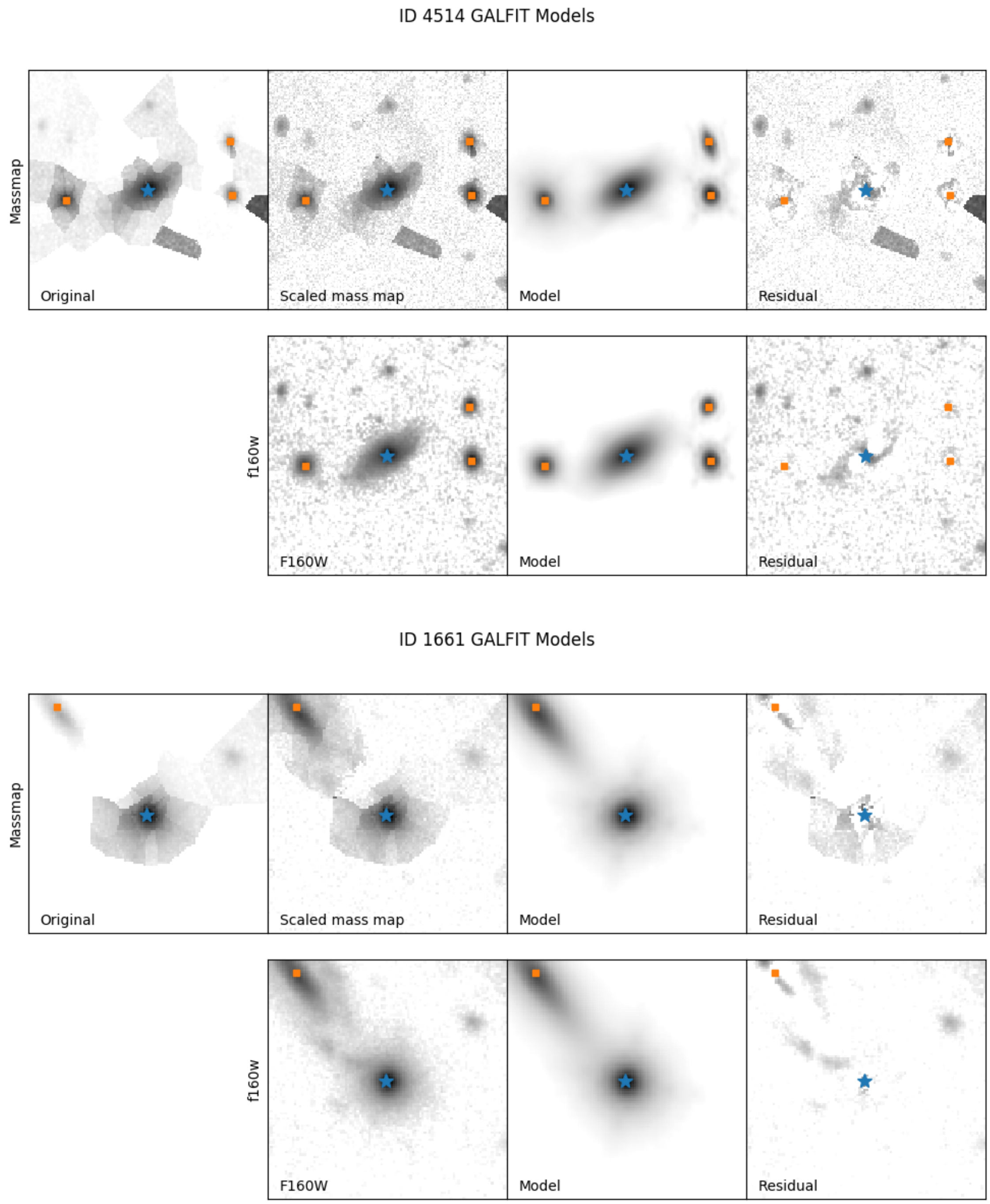

Figure (3.4) Top: An example fit from a field galaxy. Bottom: Example fit from a cluster galaxy. Note that structures such as spiral arms are not part of the Sersic fit and end up in the residual if functions specifically made for describing spiral arms are not fit. Bin residuals of stellar mass maps also end up in the residual image. The main object is highlighted by a blue star, while the other "secondary objects" are denoted by orange squares.

each object being its magnitude, and the mandatory global parameters including the zeropoint. This makes it relatively simple to fit a one component Sersic profile to each F160W cutout, the only point of failure for the surface brightness case being from not including the right amount of "secondary" objects in each cutout (sources that show up in the cutout that are not the central object that is a part of our sample, highlighted by orange squares in fig. 3.4). If too many secondary objects are fit, the solution will not converge, and conversely if not enough background objects are fit, the model computed by GALFIT is less accurate due to contamination from those sources.

3.2.2 Optimizing stellar mass maps for GALFIT

A magnitude limit was set for the secondary objects to be either < 30, or $< m_{obj} + 5$, whichever is the smaller limit, where m_{obj} is the magnitude of the central object. GALFIT also requires a sigma image to determine the "brightness" of the background and precisely how the Sersic profile for each object will look. The code can generate its own sigma image, or one can be manually created by taking the standard deviation (σ, hence the name) or the FWHM of the background flux in the image and creating a new image with the same dimensions where every pixel is that value. The GALFIT generated sigma images were used. The background was defined by the segmentation map created by SExtractor.

For the stellar mass maps, certain properties such as the tilt, major and minor axes, and the ellipticity are easily transferable from light profile to mass profile. All of the objects in our sample have similar or same values for those parameters between their stellar mass and their F160W flux. However, the stellar mass is in units of $\log(M_{\odot})$, which makes it difficult for GALFIT's algorithms to decipher as they treat each pixel value the same as flux. If the "zeropoint" in the mass map parameter file is changed into a value that makes the central object's total mass the same "magnitude" as its F160W band, then every other parameter is kept essentially the same. This is the same approach as if every pixel in the mass map was multiplied by a constant that directly converts the total mass of the central object into the total F160W flux. This scaling was applied to the stellar masses before GALFIT was run. Gaussian noise was also added to the stellar mass maps with the mean and standard deviation scaled relative to the overall stellar mass to mimic the properties of the background noise in the F160W band cutout. The added noise does not affect the total stellar mass of the object, as can be seen in Figure 3.4, but it is a necessary aid for GALFIT to properly find objects to fit in the mass maps. This streamlines the galaxy modelling process, because the same parameter file for the F160W cutouts can be used on the mass map of the same object. Without increasing the noise, the algorithm overestimates the foreground objects' intensity, and will treat every galaxy as a point spread function.

The factor by which the stellar mass is scaled would also mean the secondary objects will have very similar mass "magnitudes" to their F160W fluxes, so the secondary objects being fit can have the same initial magnitude. The bins for these fainter objects do not make them as well defined as the central object, however they do not need to have accurate Sersic profiles since GALFIT is robust enough to compensate for less accurate initial conditions while keeping the primary object as the most optimal fit. Thus, reusing the F160W parameters for secondary objects is sufficient.

As mentioned in §3.2.1, the cutout sizes need to be 20 times the SExtractor defined half-light radius for background noise estimation. This is the same cutout size for the stellar mass maps for the reason mentioned in the previous paragraph. For the majority of cases, the cutout does not contain more than 110 objects, which is the maximum number of objects that GALFIT can fit. However, not every source needs to be fit with a Sersic profile for proper background estimation and convergence, only objects with a magnitude brighter than 30 need to be fit due to the noise levels of the background. The resulting Sersic models for both the brightness fit and the mass fit are shown in figures 3.4. Out of the original 248 cluster galaxies, 235 have successful stellar mass Sersic profile fits, and 131 out of the original 141 field galaxies have successful stellar mass Sersic profile fits. The objects that fail are not biased towards any stellar mass, since the percentage of failed fits for $M_\star < 10^{9.5} M_\odot$ is roughly 9.5%, and the percentage of failed fits for $M_\star > 10^{9.5} M_\odot$ is roughly 9.1%.

3.2.3 Mass-to-Light ratio

What does modelling a Sersic profile directly onto the mass maps, without needing to convert from brightness profiles, mean for the mass-to-light ratio? Every binned group of pixels can be considered as having its own M/L ratio that was found with FAST. But there was an applied scaling that assigned more of a bin's mass to a pixel brighter in the F160W than one that is dimmer in the F160W, which can also be interpreted as a process of giving each pixel its own M/L ratio. Instead of a total ratio for the entire galaxy, in a sense, the mass maps can be interpreted as one step removed from series of resolved M/L ratio maps. The fit SED of every bin would be scaled according to the flux percentage in of each pixel in the bin making up this map.

To further expand on the implications of the methods used for stellar mass construction, in the literature most stellar mass maps are constructed using an extrapolated mass-to-light ratio. Light profiles are fit to certain infrared bands (Lang et al., 2014; Chan et al., 2016; Suess et al., 2019) that are then translated into mass using the M/L ratio. Stellar mass distributions may also be constructed with rest frame colours (Szomoru et al., 2013; Suess et al., 2019), of which the $g - r$ correlates with stellar mass. However, until this work, there had been no success with directly fitting a mass profile to a resolved mass map. The methods in the paper by Wuyts et al. (2012) are used for constructing mass maps, and with some scaling in each of the bins, a Sersic profile was directly modelled to the stellar mass with GALFIT. Since our process relies only on stellar masses from SED-fitting, the accuracy of the values solely rests with the errors of the programs used, as well as Poisson statistics. Therefore, the individual mass profiles should be a good approximation for the real stellar mass distribution of the galaxy.

Chapter 4

Results

This chapter demonstrates how the stellar mass distributions are used to examine the morphology of star-forming and quiescent galaxies in cluster and field environments. Through using parameters that describe the stellar mass distribution, a link may be drawn between certain galaxies that have different star-formation rates but similar morphology. In the previous chapter, we described how GALFIT was used to model stellar mass distributions of galaxies with a single component Sersic profile, what is referred to as a "mass profile". This is why two Sersic parameters of those mass profiles: Sersic index (n_{mass}) and half-mass radius (R_{mass}) are used to quantify morphological differences in galaxies. The galaxy sample of 235 cluster and 198 field galaxies is divided into four groups based on their star-formation rate, which is determined by their position on the UVJ colour diagram, and whether they live in a cluster(dense) or field(less dense) environment.

Before analyzing the specifics of galaxy mass profiles and the relationships of their parameters to other properties of galaxies, the methods we used must be shown to be consistent with the literature. The first section of this chapter will briefly compare the differences in light and mass profiles for our sample. This topic is well explored in the literature (i.e. Szomoru et al., 2013, van der Wel et al., 2014), so this comparison can gauge the robustness of the stellar mass maps. We discuss the differences between brightness and mass profiles (§4.1), how the mass profiles for quiescent and star-forming populations change with different masses and environments (§4.2), and how looking for outliers in the quiescent cluster population can point towards environmental quenching (§4.3). The main discussion and interpretation of these results, and their implications for quenching will be in chapter 5. The effective radii(both R_{F160W} and R_{mass}) will be reported in units of kiloparsecs, which are obtained using the galaxy's redshift and the standard values for the cosmological parameters of $\Omega_\Lambda = 0.7$, $\Omega_M = 0.3$, and $h = 0.7$.

4.1 Brightness profile versus mass profile

The infrared bands such as the H-band, which is the F160W HST band for this dataset, is sometimes used as a proxy for stellar mass. There is a steep outshining bias for more massive stars in the UV, but the IR brightness for stars of any mass scale closely with temperature, and for main sequence stars, temperature is directly proportional to mass. However, H-band and stellar mass are still the same, and the full SED of a galaxy is still the most accurate way to obtain its integrated stellar mass. This section demonstrates how the Sersic profile fits of the F160W band and the Sersic profile fits to the stellar mass maps for our complete galaxy sample result in measurable differences in their Sersic parameters.

In Figure 4.1, the Sersic parameters were plotted against one another to see how far they fall from the one-to-one line. A bulge-like quiescent galaxy is not only red in colour but has a Sersic index of $n \geq 4$ and tends to have a smaller effective radius, while a spiral galaxy is star-forming/blue, and has $n \sim 1$ and a larger effective radius. Comparing the overall trend of Sersic parameter differences requires directly plotting all of the sample's brightness profile parameters against their mass profile parameters. This is to see if there is a bias towards either light or mass for each parameter. The number of successful mass profiles and successful brightness profiles are not the same, so when making direct comparisons between these profiles for the same object, only the objects that are successful for both cases are selected.

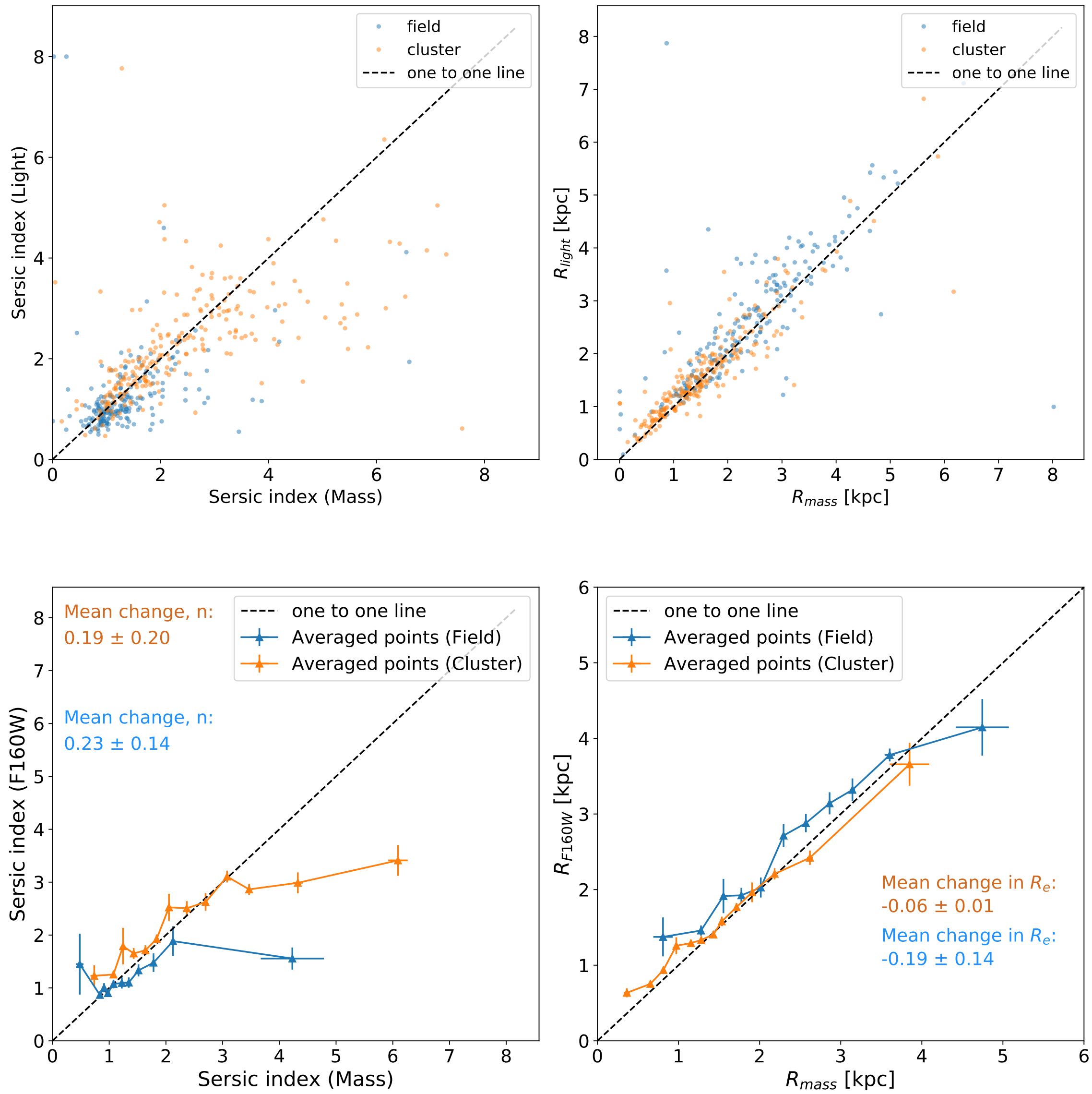

Figure (4.1) Comparisons of the same parameter between brightness profile fits and mass profile fits. The figures on the left compare Sersic indices (n) while the figures on the right compare half-light radius with half-mass radius (R_e).Each point in the bottom plots represents 17-19 objects and their average parameters are plotted with the error bars representing the standard error of each bin. These plots demonstrate how far the Sersic index or the effective radius deviates from a one-to-one relation. For both cluster and field galaxies, the slope of the Sersic index is more flat, indicating that n_{mass} is generally greater than n_{F160W}.The effective radii are more one-to-one than the Sersic indices, but for field galaxies (blue), their R_{F160W} is slightly larger than their R_{mass}.

In the bottom two panels of Figure 4.1, there are trend lines for both cluster and field, made from averaging groups of 17-19 points in both comparison spaces. These lines show the average displacement from the one-to-one black dashed line for Sersic indices(n) and effective radii (R_e). The scatter in the Sersic index relation is much greater than the effective radius relation, which translates to a greater deviation in the trend line for the plot in the bottom left panel. The overall result is n_{mass} is generally greater than n_{F160W}, while R_{mass} is smaller than R_{F160W}. The trend line for the cluster's Sersic indices tend towards smaller values for the mass profile than the light profile when $n_{F160W} \lesssim 2.5$ and $n_{mass} \lesssim 2.7$. However, n_{mass} is larger when both n_{F160W} and n_{mass} is large. For the field sample, $n_{F160W} > n_{mass}$ at $n < 1$, and $n_{F160W} < n_{mass}$ at $n > 1.3$, and in-between these two values, the Sersic indices look roughly one-to-one. This indicates that H-band fluxes might overestimate the Sersic index for disk-like galaxies but underestimate it for bulge-like galaxies.

For half-light radius versus half-mass radius, the points on the trend line are no more than 1 kpc removed from the one-to-one relation. Overall, the half-light radius is slightly larger than the half-mass radius, with almost all the points on the field galaxy's trend line being above the one-to-one relation, the biggest difference seems to be 0.6kpc. Using F160W, or the H-band flux as a proxy for stellar mass works better for the effective radius than the Sersic index, but it can still overestimate effective radii by as much as 0.6kpc. The half light radius on average being larger than the half mass radius agrees with previous results (Wuyts et al., 2010; Guo et al., 2011; Szomoru et al., 2013; Chan et al., 2016; Suess et al., 2019). The cluster sample is interesting, because galaxies with that have both small R_{F160W} and R_{mass} tend to have $R_{F160W} > R_{mass}$, while galaxies that have large R_{F160W} and R_{mass} tend to have $R_{mass} > R_{F160W}$, with the cutoff at around a Sersic index of ~ 2.5.

Parameter	**K-S statistic**	**T-value**	**F-value**
Sersic indices (cluster)	0.0940	1.605	2.576
Effective radii (cluster)	0.0798	0.703	0.495
Sersic indices (field)	0.206	1.939	3.761
Effective radii (field)	0.124	1.386	1.912

Table (4.1) Values of three two-sample statistical tests performed comparing brightness and mass profile parameters plotted in in Figure 4.1 against one another.

Parameter	standard error (F160W profiles)	p-value (K-S test)	p-value (T-test)	p-value (F-test)
Sersic indices (cluster)	0.069	0.24	0.11	0.11
Effective radii (cluster)	0.058	0.42	0.48	0.48
Sersic indices (field)	0.072	6.3×10^{-3}	0.054	0.054
Effective radii (field)	0.095	0.26	0.17	0.17

Table (4.2) The p-values of all three statistical tests performed on the data in Figure 4.1.

The Kolmogorov-Smirnov test for two samples, the T-test, and the F-test were applied to the cluster and field Sersic indices and effective radii value. All the values of each of the three statistical tests are listed in Table 4.1, and the p-values for each test are listed in Table 4.2, along with the standard error of the F160W profiles' parameters for comparison. If we adapt a significance value of $\alpha = 0.05$, then it's clear that aside from the field Sersic indices, the other parameters are greater than 0.05. The p-values of the field Sersic indices based on the T-test and F-test are close to 0.05 but still slightly greater. Statistically speaking, the Sersic profile of a stellar mass distribution is not distinguished enough from the F160W brightness profile. The values of the statistical tests show that the field Sersic indices have the largest K-S statistic, T-value, and F-value. The K-S statistic is the maximum difference between two samples, the T-test is the difference between their means, and the F-value is the ratio of their variances. In general, the larger these three values are, the more likely the samples are drawn from different populations. From these tests, we can see that the difference between the means, using the T-value column in Table 4.1, that the differences between the means are greater for Sersic indices than for effective radii, and the F-values follow the same pattern. This also means the difference in the variances between the two samples Sersic indices, one from stellar mass, one from H-band fluxes, is also greater than the effective radii. The values in Table 4.1 and 4.2, as well as the trend lines in Figure 4.1, show that H-band flux and stellar mass are closely matched in effective radii but the Sersic indices of the H-band profile may not be representative of the stellar mass profiles' Sersic indices. The trend line in Fig. 4.1 indicates stellar mass Sersic indices should be larger than H-band profile Sersic indices. In the field galaxies sample, that difference could be statistically significant enough to dispute the null hypothesis.

4.1.1 Differences in Sersic parameters by stellar mass

The trends in the Sersic parameters of the F160W light profile and the stellar mass profile have a relationship with the total stellar mass of the galaxy. It is still useful to see how both samples of parameters change with stellar mass, even though the previous section did not confirm that their differences were statistically significant. Cluster and field objects are grouped into stellar mass bins with a width of $0.5\log(M_{\odot})$ and the average Sersic index and effective radius of each stellar mass bin are plotted in Figure 4.2. There are separate lines representing the mass profile parameters or the F160W profile parameters (which are lighter in colour to the mass profile plots). Each mass bin shows almost consistently higher Sersic indices in the stellar mass regime,

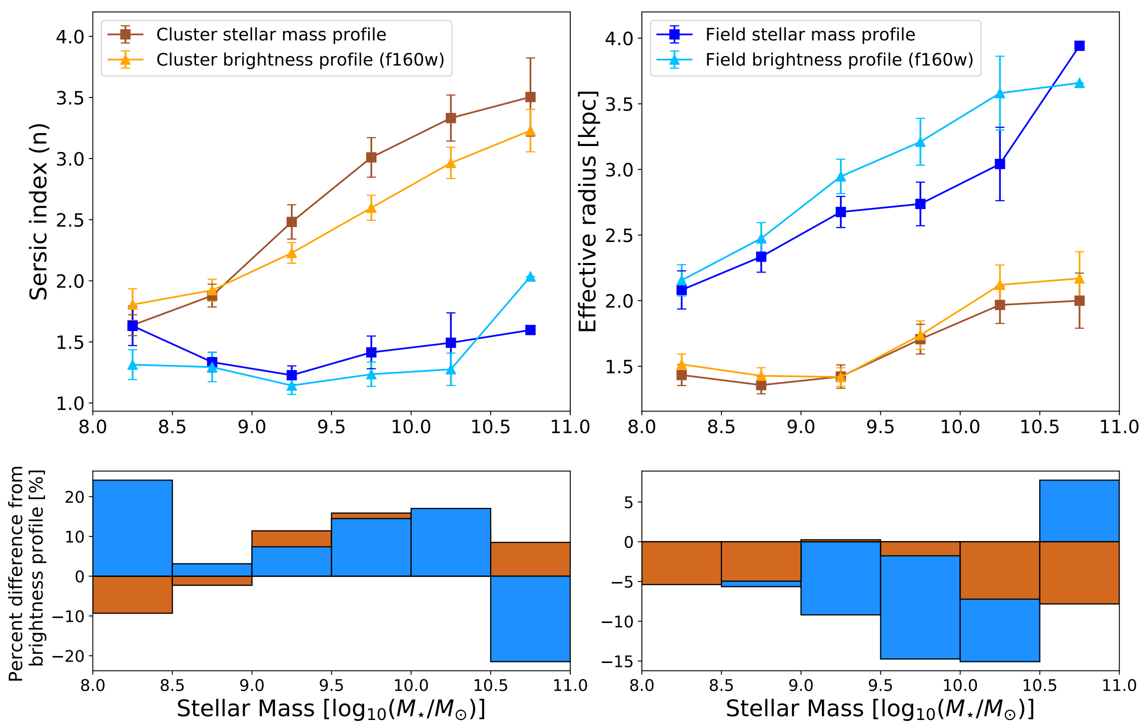

Figure (4.2) Light profile and mass profile parameter distributions when the cluster and field populations are divided into stellar mass bins of 0.5 dex width. *Left:* Mean Sersic index per stellar mass bin, with standard error. *Right:* Mean effective radii per stellar mass bin, with standard error. Histograms in bottom row represent percentage difference between mass and F160W profiles for each mass bin.

and smaller half-mass radii than half-light radii, although there is some overlap in the error bars, which represent the standard error of the distribution. The sample has a mass range of $10^8 M_\odot \leq M_* \leq 10^{11} M_\odot$.

There is no mass bin where the average R_{mass} and R_{F160W} differs by more than 0.3 kpc or 15%, as the bottom right panel shows.[1] This less dramatic change for these Sersic parameters could be a result of averaging a larger number of objects per bin when grouping by stellar mass. It still remains apparent from Figures 4.1 and 4.2 that light profile parameters and mass profile parameters have more consistent relationships with stellar mass than with each other. This seems to show that the F160W brightness profile of galaxies (at $0.25 < z < 0.6$) is generally more spatially dispersed than the true stellar mass distribution.

For the cluster sample, the greatest difference in Sersic index is about 15.87% in the $9.5 - 10$dex bin, and a 7 % difference in effective radius in the 10.5-11.0dex bin. For the field, discounting the last bin with only one point, the greatest difference is 11.46% in Sersic index, which is in the 10.0-10.5dex bin, and -12.60% in effective radius in the 9.5-10.0 dex bin. This is not as drastic of a decrease in effective radius as in previous results. For example, Szomoru et al. 2012 found a 25% decrease between the half-light radius and half-mass radius, but the redshift range in Szomoru et al. (2013) is $0.5 < z < 2.5$. Their sample includes galaxies of a much higher redshift than this work, which is $0.25 < z < 0.6$. Galaxies at high redshift, especially around $z \sim 2$ are undergoing much higher rates of star formation than at later times, which would mean higher flux but less stellar mass. The Sersic index difference we found still demonstrates stellar masses are much more concentrated than their infrared brightness profile would indicate. It is worth noting that these differences are still well within 1σ of each other. It seems that for cluster galaxies with $M_\star \lesssim 10^{9.5} M_\odot$, the mass profile becomes *less concentrated* than the light profile, but the distribution of the mass profile is still smaller overall.

[1] The largest stellar mass bin at $10^{10.5} M_\odot \leq M_\star < 10^{11} M_\odot$ appears to contradict the general trend for the field galaxies, but there is only one object from the field population in that bin, which makes it statistically insignificant.

4.2 Mass profile differences in quiescent cluster galaxies

This section describes how galaxies are classified based on star formation and environment in order to find out how stellar mass profiles are affected by those two factors combined.

4.2.1 Dividing field and cluster into star-forming and quiescent populations

The cluster and field samples are divided into quiescent and star-forming based on their position on the UVJ diagram (fig. 4.3). The UVJ diagram is a colour-colour diagram commonly used to distinguish star-forming galaxies from quiescent galaxies. The $U - V$ colours (rest frame U-band magnitude minus rest frame V-band magnitude) are plotted against $V - J$ colours (rest frame V-band magnitude minus rest frame IR), and this results in red-sequence/quiescent galaxies residing in the upper left corner of the diagram, the dusty star-forming galaxies in the upper-right corner, and the blue star-forming galaxies in the bottom half of the plot. The boundaries between star-forming and quiescent for the UVJ diagram are the same as from Shipley et al. (2018), which are defined by the equations

$$U - V < 1.3 \text{ for } V - J < 0.75 \ , \tag{4.1}$$

$$U - V < 0.8(V - J) + 0.7 \text{ for } (V - J) \geq 0.75 \ . \tag{4.2}$$

The purpose of dividing the sample into different types defined by both their environment and their star-formation rate is for two purposes. Firstly it shows how environment on its own affects the percentage of galaxies that are quiescent. Secondly, the main point of comparison are the Sersic parameters n_{mass} and R_{mass}, which are used in this work to quantify *morphological differences* between types of galaxies. This classification ensures the effects of environment and SFR on morphology is also measured accurately.

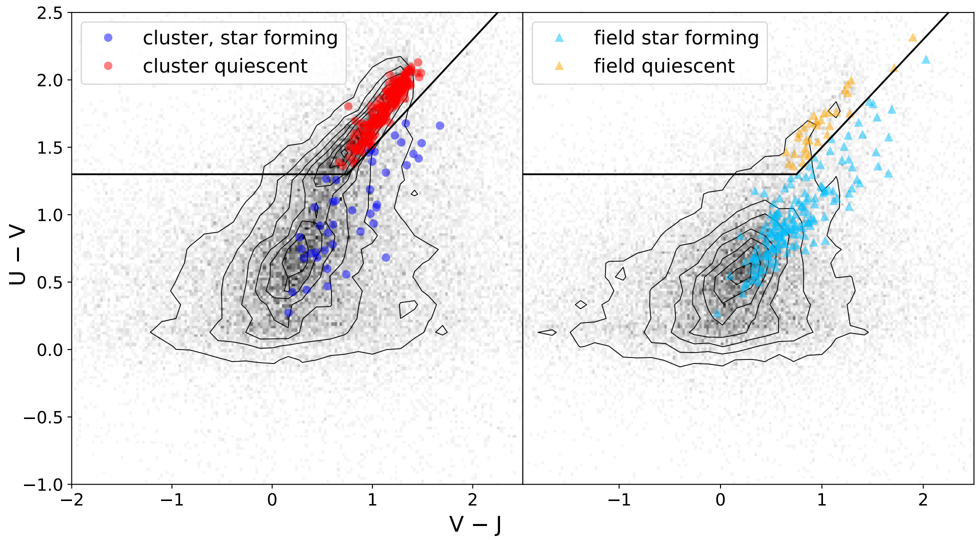

Figure (4.3) The UVJ diagram for cluster galaxies (left) and field galaxies (right). The contours show U-V vs. V-J for the entire catalog, while the red/orange points are the QC and QF galaxies in our sample, and the dark blue/light blue points are the SFC and SFF galaxies respectively. The boundaries for the UVJ diagram are from Shipley et al. (2018).

Figure 4.3 shows the UVJ colour diagram where the star-forming and quiescent galaxy samples are defined for both cluster and field. The larger coloured points are the distribution of our sample. The quiescent cluster sample will be referred to as QC, the star-forming cluster sample as SFC, the quiescent field sample as QF, and the star-forming field sample as SFF. There are 192 QC galaxies, 43 SFC galaxies, 114 SFF galaxies, and 17 QC galaxies. The low number of SFC and QC galaxies in our sample means small number statistics may bias certain measurements for those groups. First, we find the overall average n_{mass} and R_{mass} for each of the four classifications. The histogram of Sersic index and half-mass radii distributions is plotted in Figure 4.4. The purpose of these distributions is to show the variety in Sersic parameters within a single type. The star-forming field (SFF) galaxies have an average $n_{mass} \sim 1.28 \pm 0.06$, and the star-forming cluster (SFC) galaxies have an average $n_{mass} \sim 1.48 \pm 0.10$. In Fig. 4.4, the star-forming galaxies do not have any objects with $n_{mass} > 4$, and the vast majority fall between a Sersic index of 0.5 and 2. This confirms the star-forming subgroups as majority disk-like, since a Sersic profile with $n = 1$ describes a purely exponential disk (see §3.2). The average half mass radius for galaxies classified as SFC is slightly smaller than SFF galaxies, with star-forming galaxies in the field having an average R_{mass} of 2.48 ± 0.10kpc while SFC galaxies have an average R_{mass} of 2.13 ± 0.15kpc. On the whole, star-forming galaxies are slightly smaller in clusters than in the field.

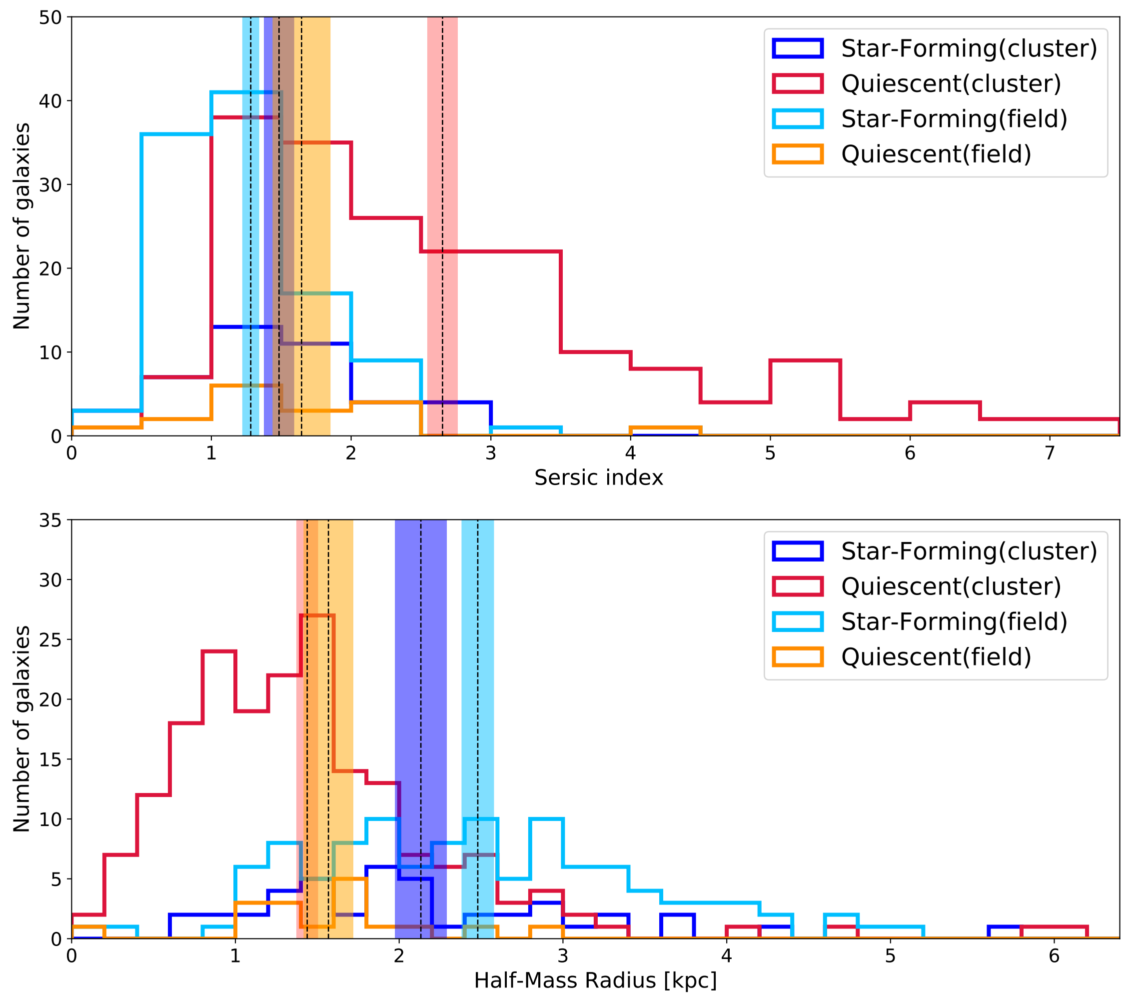

Figure (4.4) Histogram of distribution of Sersic indices(*top*) and half-mass radius(*bottom*) for each environment-SFR separated sample. The mean of each distribution marked by a dotted line with the shaded region representing the standard error of the mean.

The quiescent cluster galaxies' average Sersic index is $n_{mass} = 2.65 \pm 0.10$, which is somewhere between bulge-like and disk-like. QC galaxies are expected to be predominantly bulge-like, so the expected average Sersic index is closer to $n_{mass} \sim 4$. There appears to be just as many disk-like QC galaxies as there are bulge-like ones. This can be seen in the range of the QC distribution in Fig. 4.4 shown in red, where there are almost 80 QC galaxies with n_{mass} between 1 and 2. The number of QC galaxies in the $1 - 1.5$ bin rivals the number of SFF galaxies that are also in that bin. From this figure, it is already apparent that quiescent galaxies in a high density cluster environment seem to have two different morphologies that depend on stellar mass. The average Sersic index of the galaxies classified as quiescent field (QF) however, is only $n_{mass} = 1.64 \pm 0.20$, so QF galaxies are more disk-like than QC galaxies. In this sample, the galaxies that quench in the field, a low density environment, do not seem to have varying Sersic indices.

Despite the average n_{mass} for QF galaxies being close to the average n_{mass} for star-forming galaxies both in the cluster and the field, their average half-mass radius indicate that overall their sizes are closer to the sizes of QC galaxies. The average QC R_{mass} is 1.44 ± 0.06 and the average QF R_{mass} is 1.57 ± 0.15. On the whole, QF galaxies, with just one exception in our sample, have disk-like distributions. This is in contrast to the high density environment of the cluster where there are both galaxies with disk-like and bulge-like distributions. Quiescent galaxies in the field are more disk-like but have the smaller sizes like quiescent galaxies in the cluster. But note that these results are only from a sample size of 17 QF galaxies.

4.2.2 Sersic parameters that change with both mass and environment

There is also the dimension of stellar mass that can affect star formation and these parameters, but Figure 4.4 only shows the trends for Sersic parameters as they relate to star formation and environment. Since the intent is to look for whether the effects of both environment *and* stellar mass on quenching are entirely separable, the next logical step is to break down the distribution by stellar mass bins and then examine each bin's Sersic parameters. If the parameters have a trend that depends on stellar mass that only occurs in one environment, this would be evidence that environmental quenching and mass quenching may not be completely independent of one another.

Figure 4.5 presents each galaxy on a Sersic index vs stellar mass plot and a half-mass radius vs stellar mass plot. Each classification is distinguished by their colours: the dots and crosses are individual galaxies, while the lines are the average Sersic parameter for that particular stellar mass bin. These plots are meant to demonstrate how stellar mass affects the diversity of Sersic parameters for each type. For example, stellar mass does not seem to have a particularly large effect on the Sersic index distribution of the star-forming classifications, since their n_{mass} stays around a value of 1.2 to 1.5. However, it has a drastic effect on the Sersic index of QC (quiescent

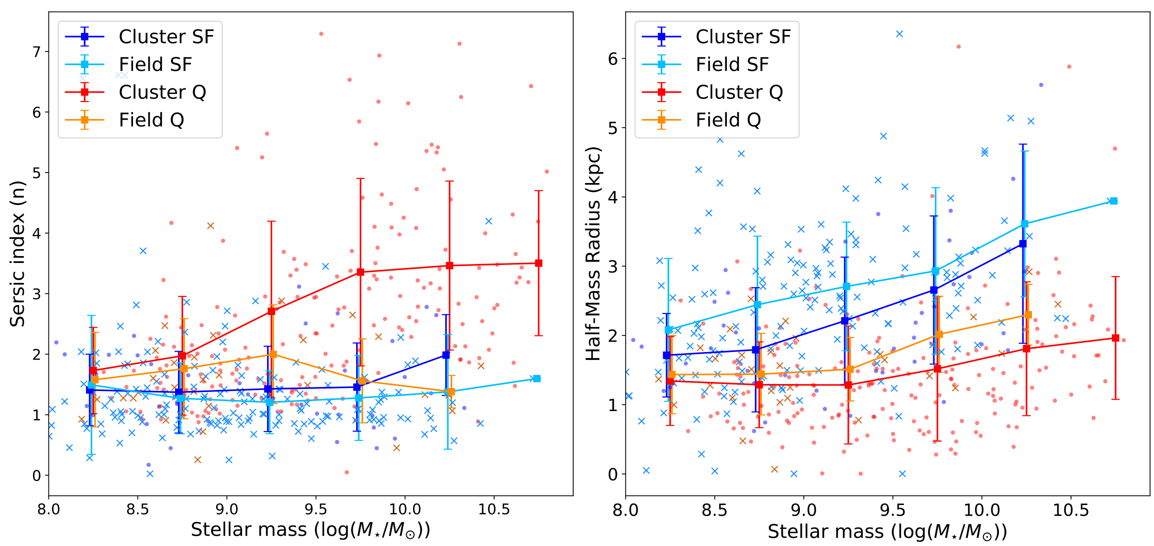

Figure (4.5) Mean Sersic index (*left*) and half-mass radii (*right*) for every stellar mass bin for each of the four environment-SFR types. The stellar mass is divided in the same way as Figure 4.2. Each point is the *mean* of the distribution in that particular stellar mass bin, and the error bars are one standard deviation from the mean. The standard deviation is used for these plots instead of standard error to show how much the individual points in each classification overlap with each other. The field population is marked with an 'x' instead of a dot to distinguish them.

cluster) galaxies. The mean n_{mass} for QC galaxies increases from $n_{mass} \sim 2$ at $M_\star = 10^{8.5} M_\odot$ to $n_{mass} \sim 3.5$ at $M_\star = 10^{9.5} M_\odot$. The trend for QF (quiescent field) galaxies seems at odds with the QC trend, which decreases with stellar mass. There are only 31 galaxies considered to be QF, so it cannot be determined whether that is a real trend with stellar mass, or if more data from additional quiescent field galaxies would result in a different distribution for this redshift. Nevertheless, there is a clear effect that stellar mass has on the Sersic index for quiescent cluster galaxies; *higher mass QC galaxies appear to be more bulge-like while lower mass QC galaxies are more disk-like.*

The right panel of Figure 4.5 is a plot of half-mass radius versus stellar mass. It has both the distribution of individual galaxies as well as the trend line representing the average at each stellar mass for the four classifications. Unsurprisingly, for every subsample, the half-mass radius increases with stellar mass, but at different rates. At the low mass end, the mean R_{mass} for each subsample is also closer together than at the high mass end. If the galaxies in each classification stay at a similar Sersic index despite increasing stellar mass, the half-mass radius should have a roughly linear relationship with stellar mass, which is seen in the two star-forming samples. The slope for the QC sample's half-mass radius vs stellar mass relation is much shallower because for the QC sample, the Sersic index increases with stellar mass. Trends in these two Sersic parameters certainly indicate that the effects of stellar mass and environment cannot be completely separated when it comes to how the morphology and star formation rate of galaxies depend on them.

4.3 Morphology of quiescent galaxies in relation to environmental quenching

The main purpose of generating the mass profiles is to explore whether the effects of environment on quenching is truly separable from the effects of stellar mass on quenching. Figure 4.5 demonstrated that the spread in the distribution of Sersic parameters can overlap between quiescent cluster galaxies and star-forming field galaxies. This section focuses on which aspects of the stellar mass range of our sample there is the most overlap between the two populations. If quiescent cluster galaxies that are disk-like skew towards a certain mass limit, that would indicate environmental quenching still depends on stellar mass.

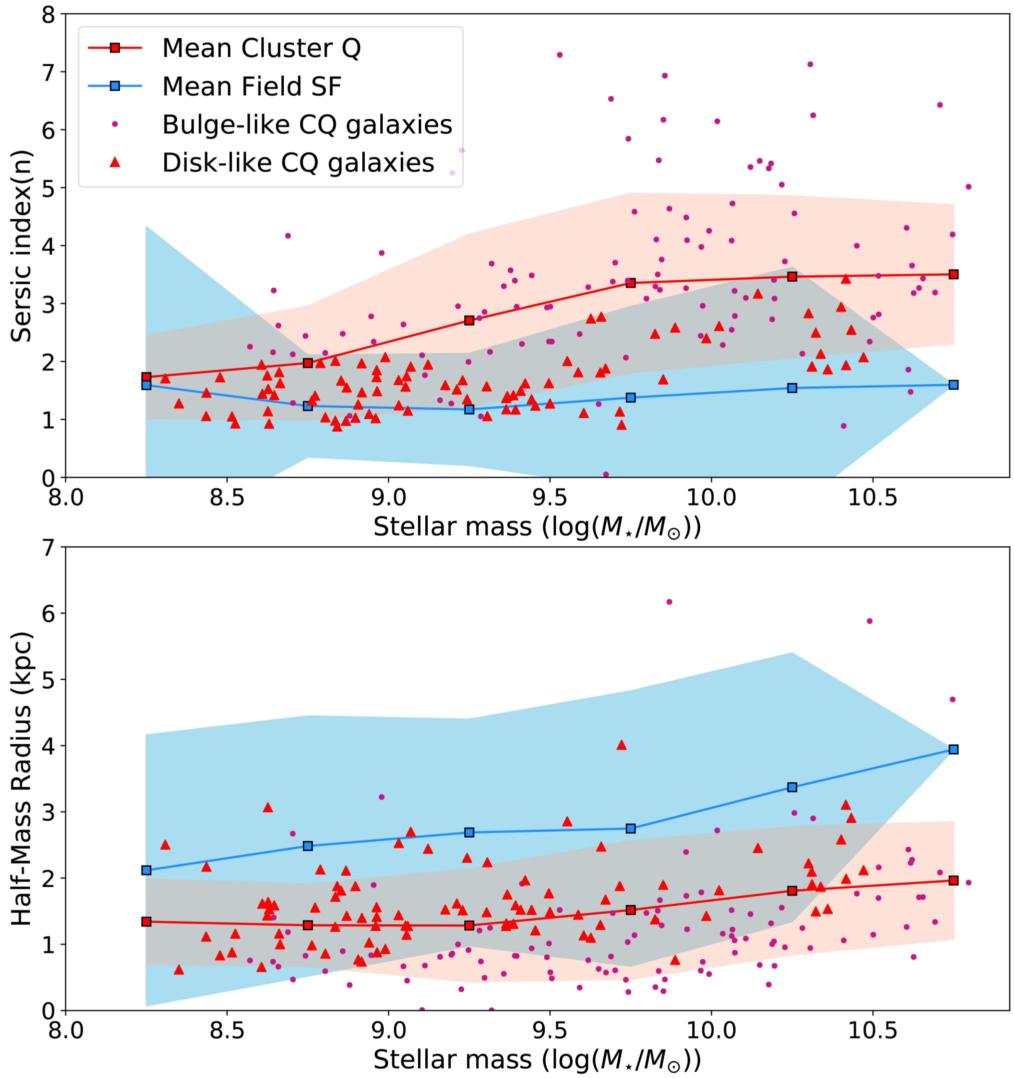

Figure (4.6) Mean parameter lines/trend lines for the QC galaxies and the SFF galaxies are shown. The light blue shaded region is within 2σ of the cyan line, and is used to separate the two QC populations based on their parameters. If a QC galaxy is within 2σ of the mean SFF parameter line (i.e. the sky blue line), then it is a quiescent galaxy with a "disk-like" morphology. These QC galaxies are marked with a red triangle, while the purplish-red circles represent quiescent galaxies with an elliptical morphology.

4.3.1 Quiescent galaxies with disk-like morphology

There must be a subset of QC galaxies that have *both* their n_{mass} and R_{mass} more like those typically seen in star-forming galaxies, the so-called "disk-like" quiescent galaxies. This can be seen in Figure 4.5, quiescent cluster galaxies generally are disk-like at $M_\star < 10^{9.5} M_\odot$ but generally bulge-like at $M_\star > 10^{9.5} M_\odot$, and star-forming galaxies tend to have Sersic indices between 1 and 2 for the entire stellar mass range. Star-forming galaxies also have a steeper $R_{mass} - M_\star$ slope than quiescent cluster galaxies, but the distribution of individual galaxies among the different classifications leads to large regions of overlap between different types. Using the average and the standard deviation as a guide, the disk-like quiescent galaxies are defined within the overlapping region. They are selected from the QC population for objects that have *both* their n_{mass} and R_{mass} within 2σ of the SFF distribution's mean for its particular mass bin. This is illustrated in Figure 4.6 where the red points that are inside the shaded light blue region are the quiescent galaxies with the right Sersic parameters. The QC objects that are excluded from this classification will be the "bulge-like quiescents", and will include some galaxies outside of the standard elliptical morphology as long as they are bulge-dominated (i.e. red nugget galaxies, which are low mass compact quiescent galaxies).

The disk-like quiescent galaxies when plotted against the entire QC distribution appear in much greater numbers at the low mass end. There are 84 such objects, which makes them around 45% of the QC sample, and 38% of all quiescent galaxies. Figure 4.7 more clearly shows the mass dichotomy between the disk-like and bulge-like quiescent galaxies by plotting a stacked histogram of the fractions that both types occupy in their stellar mass bin. Disk-like quiescents make up the majority of the quenched fraction from $10^8 M_\odot$ to $10^{9.5} M_\odot$, while bulge-like quiescents dominate at higher masses, from $10^{9.5} M_\odot$ to $10^{11} M_\odot$.

The smallest and largest mass bins notably only contain quiescent galaxies that fall into one classification, with the smallest bin having no QC galaxies of bulge-like morphology, and likewise the largest bin having no quiescent galaxies of disk-like

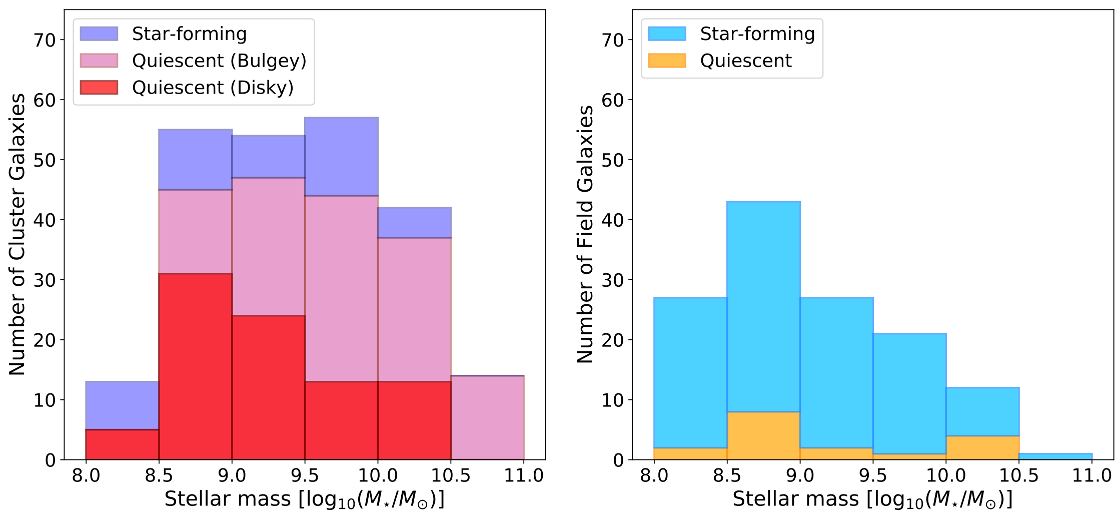

Figure (4.7) Histograms representing the total number of galaxies with the star-forming and quiescent populations stacked on top of one another to visualize the make-up for each stellar mass bin. For the cluster sample on the left, the quiescent fraction is also divided into the disk-like QC and the elliptical QC fractions, which are red and purple respectively.

Samples of stellar mass	**K-S statistic**	**K-S p-value**	**T-value**	**F-value**	**T-test p-value**
Disk-like QC vs Bulge-like QC	0.373	2.1×10^{-6}	5.52	30.5	1.2×10^{-7}
Disk-like QC vs Field Star-forming	0.208	0.024	2.42	5.87	0.015
Disk-like QC vs Cluster Star-forming	0.186	0.25	0.565	0.319	0.59
Bulge-like QC vs Cluster Star-forming	0.320	0.0028	4.84	23.4	2.3×10^{-5}

Table (4.3) Statistical tests demonstrating whether the stellar mass of disk-like QC galaxies are similar to stellar masses of other galaxy classifications. Both the test statistic values and the p-values are listed. Only the T-test p-value was listed since the F-test produces the same or slightly smaller p-values.

morphology. This explains why there are two plateaus for the QC trend line in Figure 4.5 in the previous section. For comparison, on the stacked histogram on the right of Figure 4.7, the QF to SFF ratio does not change with stellar mass. The quiescent fraction of the field galaxies does not have a stellar mass dependence, which suggests the processes that quench galaxies in cluster environments must operate differently at different masses.

The statistical robustness of these samples can be demonstrated in Table 4.3, where the stellar mass of quiescent disk-like cluster galaxies are compared against three other sample populations: the bulge-like quiescent cluster galaxies, the field star-forming, and cluster star forming galaxies. The p-values are quite small: for the K-S test, the p-value is $< 4\sigma$ significance level, and for the T-test and F-test p-value, it is $< 5\sigma$ significance level. This is quite interesting because the way the disk-like quiescents were chosen was not by stellar mass but by having similar n_{mass} and R_{mass} values as star-forming galaxies, which could indicate the disk-like and bulge-like quiescent cluster galaxies truly have different evolutionary histories, and environmental quenching seems to have a mass dependency.

Since the disk-like quiescent sample was chosen from the objects' similarities to the average parameters of star-forming galaxies, we also performed the statistical tests between disk-like quiescents and star-forming galaxies. The expectation is the p-values will be larger for both star-forming galaxies in clusters and in the field. However, even though the disk-like sample was chosen using the Sersic parameters of the field star-forming galaxies, the p-values for the K-S test and the T-test indicate that there is < 0.05 probability that their stellar masses are from the same population. Meanwhile, the p-values for disk-like QC versus cluster star-forming are above the significance level of 0.05 for both the K-S test and the T-test. For the T-test, which quantifies the difference in the two populations' means, there is a difference of less than 1, and the p-value is 0.57. This indicates that disk-like QC and cluster star-forming galaxies have stellar masses derived from a common population. The final row in Table 4.3 show that there is a significant difference in the masses between bulge-like QC and cluster star-forming galaxies, which is indicated in their p-values. This could be evidence that the method of quenching that transforms star-forming galaxies into disk-like quiescent galaxies preserves their stellar mass, but the quenching method that transforms star-forming galaxies into bulge-like quiescents alter their stellar mass significantly, meaning the quenching mechanism was either merger-based or triggered starbursts (enormous star-formation over a short time-scale).

4.3.2 Quenching efficiency formalism

From the results presented in the previous section, it is evident that there is a morphological dichotomy between low mass cluster quiescents, which are more disk-like, and high-mass cluster quiescents, which are bulge-like. To find the underlying cause of this difference, a useful measurement is how efficient the two main causes of quenching are at transforming galaxies from star-forming to quiescent. Peng et al. (2010) utilized relative quenching efficiencies to compare mass and environmental quenching for galaxies in zCOSMOS up to $z \sim 1$. They showed from their findings that mass and environment have completely independent, or "separable" effects on quenching populations of galaxies. How they arrived at their result is through showing the mass-quenching efficiency (denoted by ϵ_m) remains constant at every density, and the environmental-quenching efficiency (denoted by ϵ_ρ) also remains constant at every mass. The *environmental* quenching efficiency is defined in Peng et al. (2010) in their Equation 3, as the measure of difference in number of quiescent galaxies between two regions of space with different overdensities. We write the equation for environmental-quenching efficiency as

$$\epsilon_\rho(\rho, \rho_0, m) = \frac{f_q(\rho, m) - f_{red}(\rho_0, m)}{f_{blue}(\rho_0, m)} \quad , \tag{4.3}$$

where ρ_0 is the reference density, $f_{red}(\rho_0, m)$ is the red sequence/quiescent fraction at the reference density at a certain stellar mass m, $f_{blue}(\rho_0, m)$ is the blue cloud/star-forming fraction at the reference density, $f_q(\rho, m)$ is the quiescent fraction at environmental density ρ.

Every fraction is defined in relation to the reference density, so that if different environments make quenching "more efficient", then ϵ_ρ would increase to represent this change. A positive ϵ_ρ represents the amount of quiescent galaxies in their current environment that would have stayed star-forming if it was in the reference environment. This is why it is defined in reference to $f_{blue}(\rho_0)$ rather than $f_{red}(\rho_0)$. If changes in stellar mass also affects environmental quenching, then the efficiency ϵ_ρ would have a non-constant relationship with stellar mass as well. Peng et al. had found for galaxies at $0.3 < z < 0.6$ in zCOSMOS, that their environmen-tal and mass-quenching efficiencies were relatively constant with respect to stellar mass.

Quenched fractions and environmental-quenching efficiency(ϵ_ρ) as defined in Equation 4.3 are plotted as a function of stellar mass $M_\star$ in Figure 4.8 and Figure 4.9 respectively, to show how for fixed environments the fraction and the efficiencies change with stellar mass. If $\epsilon_\rho(M_\star)$ stays constant, then environmental quenching for those galaxies does not depend on stellar mass. That would mean mass quenching and environmental quenching are two effects that are completely independent and separable. For the cluster, the quenched fraction is also broken up into disk-like fraction and bulge-like fraction, and the two QC types also have separate quenching efficiencies. Since this sample has only two environments, ϵ_ρ is chosen to be the field environment, which is why $\epsilon_{env,field}$ is zero for all $M_\star$. However, Peng et al. were only able to probe galaxies at a mass range of $10^{10.2}M_\odot$ to $10^{11}M_\odot$, while there is a much larger range here. In the range of $10^{9.5}M_\odot$ to $10^{10.5}M_\odot$, the ϵ_ρ and f_q are more or less constant.

4.3.3 Disk-like vs bulge-like quenching efficiencies

Although Peng et al. (2010) probed a similar range of redshifts to this work (they have a sample of galaxies from zCOSMOS in the range of $0.3 < z < 0.6$), the quenching efficiencies were found to be constant at that redshift range. The stellar mass range that Peng et al.'s sample had at that redshift was only from $10^{10.2}M_\odot$ to $10^{11}M_\odot$. Looking at the ϵ_ρ plots in Figure 4.9, the quenching efficiency of the entire cluster sample does appear to be relatively constant in the range $10^{10}M_\odot < M_\star < 10^{11}M_\odot$. But the rest of the ϵ_ρ for the total cluster sample contradict the idea that effects of mass and environment on quenching are entirely separable because there is definitely an overall increasing slope that is quite steep from $10^8M_\odot < M_\star < 10^9M_\odot$, as well as the slopes of the quenching efficiencies for the disk-like and bulge-like galaxies.

Recently, papers such as Balogh et al. (2016), Lin et al. (2017), and Pintos-Castro et al. (2019) all seem to suggest that there is a mass-dependent component to environmental quenching, especially as redshift increases. This fact, in addition to the results presented in this chapter, suggests that environmental quenching and mass/self quenching leads to quiescent galaxies that have different morphologies. This

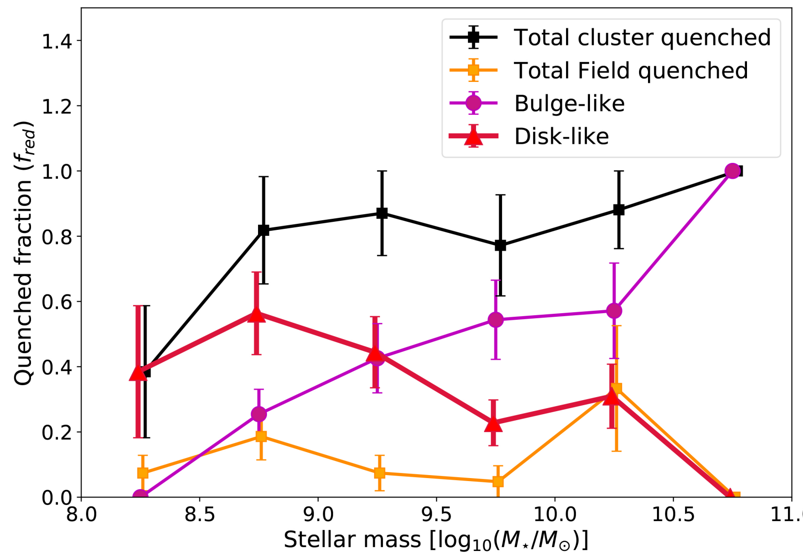

Figure (4.8) Quiescent fraction for cluster and field, with the purple line representing the bulge-like fraction, and the red representing the disk-like fraction. Since these are fractions, the error bars represent Poisson errors for each group with division error propagation. These plots show that the morphology of quiescent galaxies depends on stellar mass.

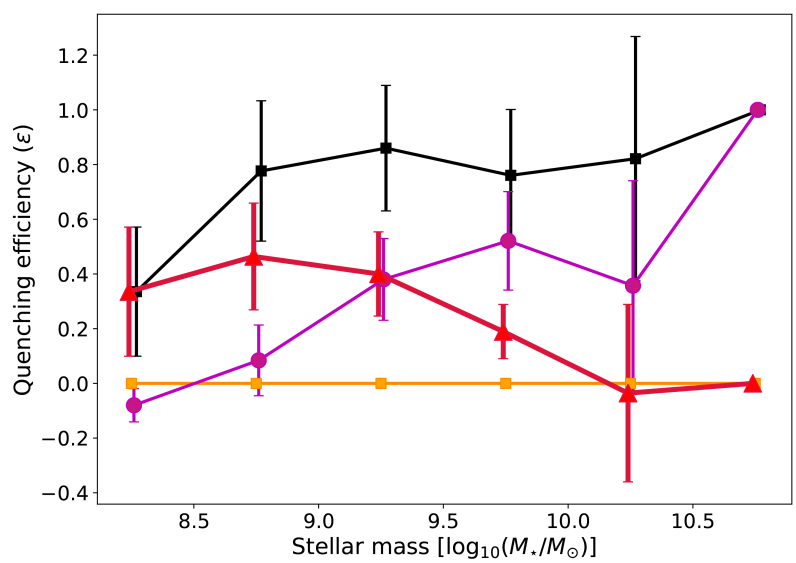

Figure (4.9) Plot of environmental-quenching efficiency as defined in Peng et al. (2010), using the field sample as the reference environment (ρ_0 in Equation 4.3). The error bars are propagated Poisson errors. These plots show that the increase in mass quenching and decrease in environmental quenching definitely depends on the stellar mass.

could indicate that disk-like quiescent galaxies that retain the morphology of star-forming galaxies were environmentally quenched through ram pressure stripping (see §5.3).

Another interesting feature of the ϵ_ρ-$M_\star$ plot is when the efficiencies match the field ϵ_ρ for the two types of bulge-like and disk-like quiescents. For bulge-like QCs, ϵ_ρ is lowest when it is at the field efficiency level, and likewise for the disk-like QC efficiencies. It is either greater than the field ϵ_ρ or they are roughly the same as the field efficiency. If the disk morphology quiescent galaxies were quenched environmentally, and the bulge-like quiescents are quenched by mass, i.e. self quenching, then this means existing in a cluster environment enhances self-quenching as well as environmental quenching. This confirms the idea proposed in earlier sections of the chapter, that the two processes operate at different stellar masses.

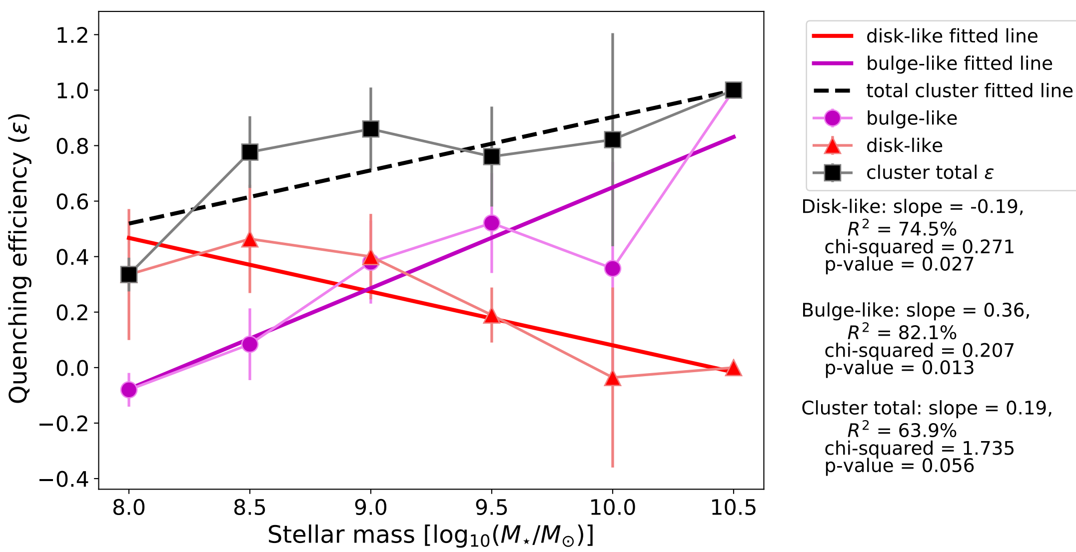

Figure (4.10) Lines of best fit to disk-like, bulge-like, and total cluster quenching efficiency ϵ_ρ. Since these efficiencies are defined relative to the field quenching efficiency, a slope of zero would indicate stellar mass has no effect on environmental quenching. On the right side of the figure, R^2 and χ^2 values showing goodness of fit, and p-values for a null hypothesis of zero are displayed.

To confirm that the slopes for the quenching efficiencies are truly distinct, trend lines were fit to the disk-like and bulge-like ϵ_ρ values from Figure 4.9. A least-squares linear regression analysis was performed using the SciPy function `lin_regress`, to obtain the slope and y-intercepts of the line. The R^2 coefficients of determination and χ-squared values are to demonstrate the goodness of fit of the trend lines. The two-sided p-values are from a Wald test, for which the null hypothesis is a slope of zero. These are displayed in Figure 4.10 along with the plot of the best fit lines. The correlation coefficients for the fitted lines are reasonable, and the p-values are < 0.05, which shows that in general, disk-like quenching efficiency is decreasing with stellar mass, and bulge-like quenching efficiency is increasing with stellar mass. This demonstrates that environmental quenching that produces different morphologies is sensitive to stellar mass, and the two morphologies of quiescent galaxies in the cluster could have arisen from different quenching processes. What is also interesting is the two slopes of the different quenching efficiencies do not cancel out, since the slope for disk-like ϵ_ρ is -0.19, but the slope for bulge-like ϵ_ρ is 0.36. This would mean there is an overall positive slope for the total quenching efficiency for cluster galaxies. Indeed, if we fit a line to the total quenching efficiency for clusters as a function of stellar mass, there is a slightly increasing slope of 0.19. While this linear fit is less robust than the disk-like and bulge-like trend lines, it still shows that even considering the quenched cluster population as a whole, and not divided into disk-like and bulge-like, there is still a weak stellar mass dependence in its ϵ_ρ, and that Peng et al.'s conclusion that ϵ_ρ is independent of stellar mass does not apply for this sample.

Chapter 5

Discussion

In this chapter, we provide physical interpretations of the results presented in the previous chapter. The opposing trends in quenching efficiency of disk-like and bulge-like galaxies with stellar mass indicates that environmental quenching has a stellar mass dependency. There are numerous ways to turn off star formation in a galaxy, so the main question is which quenching method must dominate at the two ends of the stellar mass range of our sample. There were arguments made in the past, such as in Peng et al. (2010), that mass and environment have separate, independent effects on the quenching efficiency of galaxies. Our data supports a different conclusion, that those factors have interrelated effects, meaning mass and environment are not entirely separable. It appears that different methods of quenching dominate at different ranges of stellar masses, and Peng et al.'s stellar mass range for their sample at a redshift of $0.3 < z < 0.6$ is in the range $10^{10.3} M_\odot < M_\star < 10^{11} M_\odot$. Therefore, their galaxies are in the mass-quenching dominant regime. This will be explained in §5.1 and 5.2 , which summarizes the morphological consequences of different quenching mechanisms, both for self/mass-quenching and environmental quenching. §5.3 focuses on ram pressure stripping, the method we believe dominates at the lowest masses, from $10^{8.0} M_\odot$ to $10^{9.5} M_\odot$. All of this is to show that there is a clear dependence on stellar mass for the quenching efficiency of galaxies in clusters, and that stellar mass and environment both play a role in turning off star formation that is not separable.

5.1 Dichotomy of quenching in cluster environments

We have shown that sizable portion of our sample are quiescent cluster galaxies that have stellar mass distributions that fall within 2σ of the star-forming field galaxies within their respective mass bins. These disk-like quiescent galaxies dominate the number of galaxies at $M_\star \lesssim 10^{9.5} M_\odot$. However, the majority (around 55%) of the quiescent galaxies are still morphologically quite different from star-forming galaxies, and they are predominantly at a higher stellar mass. This morphological difference, which is measured with the Sersic index and effective radius, is present in both the infrared light as well as the stellar mass distribution.

As stellar mass increases, the disk-like quenched fraction becomes the minority in clusters. Assuming that stellar mass remains conserved, self-quenching will come to dominate over environmental quenching. This is supported by the QC $M - n_{mass}$ relation becoming constant when $M_\star \gtrsim 10^{9.5} M_\odot$. In addition, the QC mass-size relation (which is the stellar mass to half-mass radius plot on the right side of 4.5), has a relatively consistent slope in the same mass range, confirming that the constant n_{mass} observed is not a quirk of the distribution, but quiescent cluster galaxies in this mass range seem to be preferentially self-quenched. Self-quenching generally refers to a galaxy's internal processes that turn off star formation, and does not depend on the number density of galaxies in the surrounding environment. These processes operate by either removing star-forming gas on a short time scale (i,e, through AGN or SN feedback) or a low star forming efficiency where the gas within the galaxy cannot form stars (i.e. disk instabilities). Self-quenching mechanisms can sometimes be triggered by minor or major mergers, which may be an additional factor as to why morphological transformation is dominant at higher stellar masses.

Given the findings outlined in chapter 4, and the very high overall quenching efficiency, the possibility that there may be morphological transformation at all stellar masses should be considered. There are still bulge-like quiescent objects with stellar masses from $10^{8.5} M_\odot < M_\star < 10^{9.5} M_\odot$. There are quenching processes that only occur in a cluster but increase the bulge-to-disk ratio of galaxies, which generally stem from tidal effects. Tidal stripping, as opposed to ram pressure stripping, does act on the stars of an infalling satellite galaxy in a way that would disrupt the star-forming disk (Merritt, 1984; Christlein & Zabludoff, 2004). Tidal heating is a process where tidal forces increase the random motion of stars, also called kinematic heat, in a satellite galaxy, making its shape more bulge-like. There is also the possibility of several quenching methods occurring at the same time for these galaxies, which results in the variety of Sersic indices and spread in half-mass radius seen in the cluster quiescent sample. In simulations, tidal effects were shown to produce S0s from galaxies with AGN (Seyfert galaxies), while ram pressure stripping primarily affects the outer regions (Byrd & Valtonen, 1990). If tidal effects trigger AGN, and that leads to AGN feedback, then this is a viable quenching pathway for the quiescent galaxies on the more massive end of our sample (Behroozi et al., 2010; Moster et al., 2010). Some of the low mass but high Sersic index objects may also be red nuggets that formed and quenched at an earlier time and fell into the cluster (Zolotov et al., 2015). Red nugget galaxies are low mass compact galaxies that are quiescent.

5.2 Framework of environmental quenching

Environmental quenching, mostly through ram-pressure stripping is dominant at low stellar mass, and mass/self-quenching is dominant at high stellar mass. The reason that lower mass galaxies are more likely to be environmentally quenched can be explained by how ram-pressure stripping operates. As Gunn & Gott explains, the ram pressure comes from the gas density of the intracluster medium (or ICM) and the velocity of the infalling galaxy (equation 61 in Gunn & Gott).

$$P_{ram} \approx \rho_{icm} v^2, \tag{5.1}$$

There is a restoring force from the galaxy's disk that counteracts P_{ram} (equation 62 in Gunn & Gott), which depends on the surface mass density of both the stars (σ_s) and the gas (σ_g).

$$F_{restore} = 2\pi G \sigma_s \sigma_g, \tag{5.2}$$

The stellar mass maps show that the surface densities of lower-mass galaxies are lower than high-mass galaxies. This seems to explain why the $n_{mass} - \log(M_{\star})$ relation for

QC galaxies is not just linear, but has two plateaus. Since the $R_{mass} - \log(M_\star)$ relationship only has a shallow upward slope, that implies the surface density of QC galaxies that have $M_\star \gtrsim 10^{9.5} M_\odot$ is greater, and thus they are less prone to being ram pressure stripped. But the QC galaxies are already quenched, so their Sersic parameters do not reveal what their precursor properties would have been before quenching occurred. Examining the star-forming galaxies both in the field and in the clusters, the SFF n_{mass} does not depend on stellar mass while the SFF R_{mass} is proportional to $\log M_\star$. The star-forming galaxies in the cluster seem to have similar relationships with stellar mass, except the more massive SFCs have a slightly higher Sersic index ($n_{mass} \sim 2$ instead of $n_{mass} \sim 1.5$). If we assume the precursors to the QC sample were morphologically similar to the SFF or SFC populations, then their surface mass density had only a weak dependence on stellar mass. This implies the possibility that RPS operates equally among all masses of galaxies but other quenching methods dominate over RPS over a certain stellar mass limit.

In addition to surface mass density, there is also the stellar mass - halo mass relation. Galaxies with lower stellar mass tend to have a lower stellar mass to halo mass ratio (Moster et al., 2010; Behroozi et al., 2010) a piece of information that would not have been known by Gunn & Gott when they published their findings. The dark matter surface density is also less dense where the gas is located, and this also contributes to quicker depletion of gas for low mass galaxies. Although apart from gravitational effects, dark matter is collisionless, so it cannot be affected by ram pressure stripping.

5.3 Ram pressure stripping and morphology

As a galaxy falls through the ICM, the stars remain in place while the gas is stripped away by interactions of the gas in the galaxy's halo with the gas in the ICM. There is some geometry involved to determine how much of the gas is stripped off the galaxy; edge on infalling disks would lose $\sim 50\%$ less gas than face on disks, according to Abadi et al. (1999), who applied the model of ram pressure stripping (RPS) described in Gunn & Gott to N-body simulations of disk galaxies. In general, they find that at a certain radius, if the ram pressure exceeds the restoring force per area, then the gas at that radius will be stripped off. At first glance it does not appear that ram pressure stripping should preferentially quench lower mass galaxies since none of the terms in equation 5.1 or 5.2 necessarily depend on mass, only mass densities. However, as demonstrated in Abadi et al. (1999), the existence of this "stripping radius" means that lower mass galaxies will be quenched by ram pressure much more easily than higher mass galaxies because the former are smaller, have less surface mass density, or both. This connects to the results that the disk-like quiescents are mostly lower mass, and being ram pressure stripped would maintain their disk-like morphology.

This also makes sense in terms of the velocity that an infalling galaxy will have. Galaxies of any mass falling into a cluster will have similar velocities, but a less massive galaxy will have a smaller potential well, and the gas can escape it more easily at the same v than from a more massive galaxy with a larger gravitational potential well. Escaping gas would not alter the physical distribution of the stellar mass content within the galaxy, so it keeps the same distribution as it had before it was ram-pressure stripped. The galaxy eventually exhausts any remaining gas left in a short amount of time (around 10^7 years), and the galaxy is now quiescent. Since σ_s remains intact, the stellar mass distribution retains n_{mass} close to 1. Again, the finding that disk-like quiescent galaxies are mostly low mass is supported by the ram pressure stripping model.

Meanwhile, satellite galaxies of a higher mass would be more likely to self quench, as ram-pressure stripping would not have much of an effect on getting rid of their cold gas. How is this supported by models of self quenching? Feedback from AGN is a likely candidate for mass quenching and star-forming massive galaxies of $M_\star \gtrsim 10^{11} M_\odot$ have been shown to have larger bulge-to-total ratios, even for stellar mass distributions (Lang et al., 2014), adding more feasibility to the idea that more massive galaxies undergo a morphological change during quenching. It is also clear that being a cluster member increases the rate of quenching in general, not just because of environmental quenching for the lowest mass satellite galaxies but also for higher mass galaxies that should be in the mass-quenching regime (see §4.3.3). It could be that most massive galaxies are already quenching or quiescent before they fall into a larger halo (e.g. van den Bosch et al. 2008), but these galaxies should have a mass of $M_\star \gtrsim 10^{11} M_\odot$, which is beyond the upper limit of our maximum stellar mass. There are studies that find denser environments increase the rate of minor mergers,which encourages bulge growth, but they are not significant enough to explain the drastic increase in quiescent galaxies in clusters.

Wetzel et al. (2012) show current quenched fractions do not correlate to current density because the quiescent galaxies would have quenched at an earlier time when the density is different. If there were a larger number of quiescent field galaxies, the same analysis could be performed where the mass profile properties of the star-forming galaxies is used to divide the quiescent field sample into two morphological groups that could then be compared against the two quiescent cluster groups. Perhaps the quenching enhancement in the mass quenching regime disappears when there are more quenched field galaxies. An important note is that quenched fractions are highly dependent on redshift, as more galaxies become quiescent over time. It is generally accepted that in the local universe, mass and environmental quenching are completely separable, but in the $z \sim 1$ universe, these quenching methods are less separable for $M_\star \lesssim 10^{11} M_\odot$. Perhaps the separability of mass and environment on quenching affects lower and lower stellar masses as we approach $z \sim 0$. Studying this would require applying our methods to a much larger survey of intermediate and high redshift galaxies.

5.4 Future work

As stated in §3.2, work can be made on improving the uncertainties for the background values in our stellar mass maps. Voronoi binning works well for high signal-to-noise, which means foreground stellar mass is quite accurate, as can be seen back in figure 3.3, but more consistent backgrounds will result in better Sersic profile models. A logical next step is to perform bulge-disk decomposition on the stellar mass maps, which simply requires two Sersic profiles, one to fit the bulge and one to fit the disk. B/T decomposition has been done on stellar masses in the past, where the mass distributions were defined using rest-frame colours, but with SED-fitting, the stellar masses are far more accurate. Morphology an be studied more closely with decomposition.

We have a robust algorithm for creating resolved stellar mass maps at *HST* resolution. However, as demonstrated in this paper, HST data does not have the sheer numbers of large scale surveys, and in order to understand quenching at high redshift, more survey data is needed. The limitation is the resolution is poor at $z > 1$. With the advent of better deconvolution methods, especially Finite Resolution Deconvolution (FIREDEC, Cantale et al., 2016), the method of stellar map creation described in chapter 3 may be applied to deconvolved images of high redshift galaxies.

Christlein & Zabludoff (2004) studied "late-type" galaxies (i.e. galaxies with a disk morphology) in three nearby clusters for evidence of transformation, and they found that truncation of Hα emission in the outer regions of galaxies is correlated with ram pressure stripping. They were also able to date when the stripping event occurred by comparing the radial profile of the observed gas to the i band surface brightness. A similar study can be conducted on disk-like quiescent galaxies within the clusters of the Hubble Frontier Fields.

Chapter 6

Conclusions

We created spatially resolved stellar mass maps of over 200 cluster and field galaxies in the Hubble Frontier Fields through SED-fitting the integrated flux of spatially binned images to find the underlying stellar mass. The bins were generated with a Voronoi tessellation algorithm to maximize the signal-to-noise ratio for ensuring the best-fit SED accurately represents the "true" SED. Sersic profiles were fit directly to these stellar mass maps in order to quantify their morphology in terms of two parameters: the Sersic index (n_{mass}), and the effective radius, also called the half-mass radius (R_{mass}). The purpose of creating resolved stellar mass maps for cluster and field galaxies is to study the morphological changes galaxies undergo when quenching. Sersic indices and half-mass radii of quiescent and star-forming galaxies were analyzed and compared to determine the effects of stellar mass and environment on quenching of star formation.

- There is a mass dichotomy in galaxy quenching that appears even at $0.25 < z < 0.6$, where less massive galaxies are more likely to be environmentally quenched while also retaining a disk-like morphology with mean $n_{mass} \sim 1.67$, and massive galaxies are more likely to be self quenched with a more bulge-like morphology where mean $n_{mass} \sim 3.45$. Statistical tests show the stellar masses of bulge-like and disk like quiescent cluster galaxies are distinct from one another, with $>4.5\sigma$ significance level.
- The environmental-quenching efficiency ϵ_ρ for disk-like galaxies was found to

be greater than the ϵ_ρ for bulge-like galaxies at stellar masses $M_\star < 10^{9.5} M_\odot$, accounting for $\sim$ 73.5% of quenching for galaxies with stellar masses $M_\star \sim 10^8 M_\odot$ to $10^9 M_\odot$. The environmental quenching ϵ_ρ for disk-like galaxies decreases with increasing $M_\star$, while ϵ_ρ for bulge-like galaxies increases with increasing $M_\star$.

- Mass and environmental effects are not separable at $0.25 < z < 0.55$ when it comes to how they correlate with quenching efficiency. In addition, Chapter 5 discussed other forms of environmental quenching that can change a disk-like profile into a more bulge-like profile, such as tidal heating. Tidal effects, which are related to the environmental density can also induce self quenching for more massive galaxies, such as AGN feedback.
- The mass profile Sersic indices of field galaxies were found to be greater than their H-band brightness profile Sersic indices, with a p-value of 0.054 from the T-test, and 0.0063 from the K-S test. The differences in mass profile and brightness profile Sersic indices for cluster galaxies are not as high, only 0.24 from the K-S test and 0.11 from the T-test. The half-mass radii and half-light radii for both field and cluster galaxies are not significantly different.

This leads to the conclusion that the effects of stellar mass and environment on quenching are not separable at $0.25 < z < 0.6$. Our results confirm that for environmental quenching, there is indeed a mass dependence, which agrees with the results in Balogh et al. (2016); Darvish et al. (2016); Kawinwanichakij et al. (2017); Lin et al. (2017) and Pintos-Castro et al. (2019). In addition, we also find there is a morphological dichotomy between low mass and high mass quenched satellites in clusters, which means different methods of quenching dominate at different stellar masses for the regions of the universe with the highest densities. There has been evidence that at redshifts greater than $z \sim 1$ that quenching mechanisms are not easily separated into environmental or mass quenching. This work shows that at intermediate redshifts between 0 and 1, these quenching efficiencies are different from the local universe.

Appendix A

A.1 Error Propagation

For the errors in the quiescent fraction and the quenching efficiencies which come from the quiescent fraction, the upper and lower limit derivations are from Gehrels (1986) with Poisson statistics for small numbers. The rest of the errors are either the χ-squared error of the FAST output propagated out, which contributes a mostly negligible amount of error, or the error from the GALFIT output, which is also mostly negligible. Therefore, most errors are either standard deviation or as stated before, Poisson error.

The equation for addition error propagation:

$$\sigma_z = \sqrt{\sum_{i=0}^{N} \sigma_{x,i}^2} \quad , \tag{A.1}$$

where σ_z is the error of the sum, and $\sigma_{x,i}$ is the error of one element of the sum.

The equation for multiplication error propagation:

$$\sigma_z = z\sqrt{\sum_{i=0}^{N} \left(\frac{\sigma_{x,i}}{x_i}\right)^2} \quad , \tag{A.2}$$

where σ_z is the error of the result, and $\sigma_{x,i}$ is the error of one element of the multiplication.

The equation for standard error:

$$\sigma_{SE} = \frac{\sigma}{\sqrt{n}} \quad , \tag{A.3}$$

where σ is the standard deviation of the distribution, and n is the size of the sample.

A.2 Confidence intervals for small numbers

The equations for Poisson upper and lower limits from Gehrels (1986):

$$\sigma_u = N + \sqrt{S(N+1)} + (S^2+2)/3 \tag{A.4}$$

$$\sigma_l = N\left(1 - \frac{1}{9N} - \frac{S}{3\sqrt{N}} + \beta N^{\gamma}\right)^3 \tag{A.5}$$

where N is the size of the sample, S and β are free parameters that changes depending on N and the confidence level. Gehrels (1986) contains tables for each parameter's value for $0 \leq n \leq 100$, at confidence levels of 85% to 99.995%.

A.3 T-test and F-test

The T-test and F-test determine whether the null hypothesis may be ruled out in explaining the correlation between two sets of data. The independent T-test compares the means of two independent sets to determine if they are significantly different, while the F-test is the ratio between two variances: the variance between groups, and the variance within each group.

We applied a type of T-test known as Welch's T-test, where the two population variances are not assumed to be equal.

$$t = \frac{\bar{X}_1 = \bar{X}_2}{s_{\bar{\Delta}}} \quad , \tag{A.6}$$

$$\text{where} \quad s_{\bar{\Delta}} = \sqrt{\frac{s_1^2}{n_1} + \frac{s_2^2}{n_2}} \quad . \tag{A.7}$$

s_i is the unbiased estimated of variance of each of the samples, and n_i is the size of each sample.

For the F-test,

$$F = \frac{\text{between-group variance}}{\text{within-group variance}} \quad . \tag{A.8}$$

Between-group variance, also sometimes known as the explained variance, is defined by the sum

$$\sum_{i=1}^{K} n_i(\bar{Y}_i - \bar{Y})^2/(K-1) \quad , \tag{A.9}$$

where K is the number of groups, n_i is the size of sample i, $\bar{Y}_i$ is the mean of sample i, and $\bar{Y}$ is the overall mean of the entire data set.

Within group variance, also sometimes known as the unexplained variance, is defined by the sum

$$\sum_{i=1}^{K}\sum_{j=1}^{n_i}(Y_{ij} - \bar{Y}_i)^2/(N - K) \quad , \tag{A.10}$$

where K is the number of groups, n_i is the size of sample i, $\bar{Y}_i$ is the mean of sample i, and Y_{ij} is the jth element of sample i, and N is the overall sample size (i.e. the size of every sample added together). We used the SciPy functions `ttest_ind` and `f_oneway` for the T-test and F-test respectively for the T-values and F-values, as well as their p-values in Chapter 4.

A.4 Kolmogorov-Smirnov Test

The Kolmogorov-Smirnov test (or K-S test) is used to either compare one data set against a reference probability distribution, or compare the empirical distribution function $F_n(x)$ of two samples against one another. the idea is to show if the variability of a data set can be explained by the null hypothesis, or if the difference between the reference and the sample, or the difference between both samples, is great enough that the null hypothesis can be refuted as the sole explanation. For this thesis, we used the two-sample K-S test. The D-statistic is defined as

$$D_{n,m} = \sup |F_{1,n}(X) - F_{2,m}(x)| \quad , \tag{A.11}$$

which is the maximum distance between the two samples' empirical distribution functions ($F_{1,n}(x)$ is the first sample, and $F_{2,m}(x)$ is the second sample). We used `ks_2samp` from the Python package SciPy to calculate the K-S statistic and p-values of our samples in Chapter 4.

Appendix B

B.1 Extra figures and tables

Table (B.1) *Image sources (used in this thesis only).*

HFF Field	Hubble Filters	Instrument	Survey (and source)
Abell370-clu	F275W, F336W	UVIS	PID:14209 (B. Siana)
	F435W, F606W, F814W	ACS	HFF (Lotz et al., 2017)
	F475W, F625W	ACS	PID:11507 (PI: K. Noll)
	F475W	ACS	PID:11582 (PI: A. Blain)
	F625W	ACS	PID:13790 (PI: S. Rodney)
	F105W, F125W, F140W, F160W	WFC3	HFF (Lotz et al., 2017)
	F110W	WFC3	PID: 11591 (PI: J.P. Knieb),
			PID: 13790 (PI: S. Rodney)
Abell1063-clu	F225W, F390W	UVIS	CLASH (Postman et al., 2012)
	F275W, F336W	UVIS	PID:14209 (PI: B. Siana)
	F435W, F606W, F814W	ACS	HFF (Lotz et al., 2017)
	F475W, F625W, F775W, F850LP	ACS	CLASH (Postman et al., 2012)
	F105W, F125W, F140W, F160W	WFC3	HFF (Lotz et al., 2017)
	F110W	WFC3	PID:12458 (PI: M. Postman)
Abell2744-clu	F275W, F336W	UVIS	PID:14209 (PI: B. Siana)
	F435W, F606W, F814W	ACS	HFF (Lotz et al., 2017)
	F105W, F125W, F140W, F160W	WFC3	HFF (Lotz et al., 2017)
MACS0416-clu	F225W, F390W	UVIS	CLASH (Postman et al., 2012)
	F275W, F336W	UVIS	PID:14209 (PI: B. Siana)
	F435W, F606W, F814W	ACS	HFF (Lotz et al., 2017)
	F475W, F625W, F775W	ACS	PID: 12459 PI: M. Postman
	F850LP	ACS	CLASH (Postman et al., 2012)
	F105W, F125W, F140W, F160W	WFC3	HFF (Lotz et al., 2017)
	F110W	WFC3	CLASH (Postman et al., 2012)
MACS0717-clu	F225W, F390W	UVIS	CLASH (Postman et al., 2012)
	F275W, F336W	UVIS	PID: 14209 PI: B. Siana
	F435W, F606W, F814W	ACS	HFF (Lotz et al., 2017)
	F475W, F625W, F775W, F850LP	ACS	PID: 12103 (PI: M. Postman)
	F555W	ACS	CLASH (Postman et al., 2012)
	F105W, F125W, F140W, F160W	WFC3	HFF (Lotz et al., 2017)

	F110W	WFC3	CLASH (Postman et al., 2012)
MACS1149-clu	F225W, F390W	UVIS	CLASH (Postman et al., 2012)
	F275W, F336W	UVIS	PID: 14209 PI: B. Siana
	F435W, F606W, F814W	ACS	HFF (Lotz et al., 2017)
	F475W, F625W, F775W, F850LP	ACS	PID: 12103 (PI: M. Postman)
	F555W	ACS	CLASH (Postman et al., 2012)
	F105W, F125W, F140W, F160W	WFC3	HFF (Lotz et al., 2017)
	F110W	WFC3	CLASH (Postman et al., 2012)
Abell370-par	F435W, F606W, F814W	ACS	HFF (Lotz et al., 2017)
	F105W, F125W, F140W, F160W	WFC3	HFF (Lotz et al., 2017)
Abell1063-par	F435W, F606W, F814W	ACS	HFF (Lotz et al., 2017)
	F105W, F125W, F140W, F160W	WFC3	HFF (Lotz et al., 2017)
Abell2744-par	F435W, F606W, F814W	ACS	HFF (Lotz et al., 2017)
	F105W, F125W, F140W, F160W	WFC3	HFF (Lotz et al., 2017)
MACS0416-par	F435W, F606W, F814W	ACS	HFF (Lotz et al., 2017)
	F775W, F850LP	ACS	PID:12459 (PI: M. Postman)
	F475W, F625W, F775W	ACS	PID: 12459 (PI: M. Postman)
	F850LP	ACS	CLASH (Postman et al., 2012)
	F105W, F125W, F140W, F160W	WFC3	HFF (Lotz et al., 2017)
MACS0717-par	F435W, F606W, F814W	ACS	HFF (Lotz et al., 2017)
	F105W, F125W, F140W, F160W	WFC3	HFF (Lotz et al., 2017)
MACS1149-par	F435W, F606W, F814W	ACS	HFF (Lotz et al., 2017)
	F105W, F125W, F140W, F160W	WFC3	HFF (Lotz et al., 2017)

Bibliography

Abadi, M. G., Moore, B., & Bower, R. G. 1999, Mon. Not. R. Astron. Soc., 308, 947

Baldry, I. K., Balogh, M. L., Bower, R. G., Glazebrook, K., Nichol, R. C., Bamford, S. P., & Budavari, T. 2006, Mon. Not. R. Astron. Soc., 373, 469

Balogh, M., Eke, V., Miller, C., Lewis, I., Bower, R., Couch, W., Nichol, R., Bland -Hawthorn, J., Baldry, I. K., Baugh, C., Bridges, T., Cannon, R., Cole, S., Colless, M., Collins, C., Cross, N., Dalton, G., de Propris, R., Driver, S. P., Efstathiou, G., Ellis, R. S., Frenk, C. S., Glazebrook, K., Gomez, P., Gray, A., Hawkins, E., Jackson, C., Lahav, O., Lumsden, S., Maddox, S., Madgwick, D., Norberg, P., Peacock, J. A., Percival, W., Peterson, B. A., Sutherland, W., & Taylor, K. 2004a, Mon. Not. R. Astron. Soc., 348, 1355

Balogh, M. L., Baldry, I. K., Nichol, R., Miller, C., Bower, R., & Glazebrook, K. 2004b, Astrophys. J. Lett., 615, L101

Balogh, M. L., McGee, S. L., Mok, A., Muzzin, A., van der Burg, R. F. J., Bower, R. G., Finoguenov, A., Hoekstra, H., Lidman, C., Mulchaey, J. S., Noble, A., Parker, L. C., Tanaka, M., Wilman, D. J., Webb, T., Wilson, G., & Yee, H. K. C. 2016, Mon. Not. R. Astron. Soc., 456, 4364

Bamford, S. P., Nichol, R. C., Baldry, I. K., Land, K., Lintott, C. J., Schawinski, K., Slosar, A., Szalay, A. S., Thomas, D., Torki, M., Andreescu, D., Edmondson, E. M., Miller, C. J., Murray, P., Raddick, M. J., & Vandenberg, J. 2009, Mon. Not. R. Astron. Soc., 393, 1324

Behroozi, P. S., Conroy, C., & Wechsler, R. H. 2010, Astrophys. J., 717, 379

Bell, E. F., van der Wel, A., Papovich, C., Kocevski, D., Lotz, J., McIntosh, D. H., Kartaltepe, J., Faber, S. M., Ferguson, H., Koekemoer, A., Grogin, N., Wuyts, S., Cheung, E., Conselice, C. J., Dekel, A., Dunlop, J. S., Giavalisco, M., Herrington, J., Koo, D. C., McGrath, E. J., de Mello, D., Rix, H.-W., Robaina, A. R., & Williams, C. C. 2012, Astrophys. J., 753, 167

Bellstedt, S., Lidman, C., Muzzin, A., Franx, M., Guatelli, S., Hill, A. R., Hoekstra, H., Kurinsky, N., Labbe, I., Marchesini, D., Marsan, Z. C., Safavi-Naeini, M., Sifón, C., Stefanon, M., van de Sande, J., van Dokkum, P., & Weigel, C. 2016, Mon. Not. R. Astron. Soc., 460, 2862

Bertin, E. & Arnouts, S. 1996, Astron. Astrophys. Suppl. Ser., 117, 393

Blanton, M. R. & Moustakas, J. 2009, Annu. Rev. Astron. Astrophys., 47, 159

Bluck, A. F. L., Maiolino, R., Sánchez, S. F., Ellison, S. L., Thorp, M. D., Piotrowska, J. M., Teimoorinia, H., & Bundy, K. A. 2020, Mon. Not. R. Astron. Soc., 492, 96

Brammer, G. B., Marchesini, D., Labbé, I., Spitler, L., Lange-Vagle, D., Barker, E. A., Tanaka, M., Fontana, A., Galametz, A., Ferré-Mateu, A., Kodama, T., Lundgren, B., Martis, N., Muzzin, A., Stefanon, M., Toft, S., van der Wel, A., Vulcani, B., & Whitaker, K. E. 2016, Astrophys. J. Suppl. Ser., 226, 6

Brammer, G. B., van Dokkum, P. G., & Coppi, P. 2008, Astrophys. J., 686, 1503

Brinchmann, J., Charlot, S., White, S. D. M., Tremonti, C., Kauffmann, G., Heckman, T., & Brinkmann, J. 2004, Mon. Not. R. Astron. Soc., 351, 1151

Bruzual, G. & Charlot, S. 2003, Mon. Not. R. Astron. Soc., 344, 1000

Byrd, G. & Valtonen, M. 1990, Astrophys. J., 350, 89

Calzetti, D., Armus, L., Bohlin, R. C., Kinney, A. L., Koornneef, J., & Storchi-Bergmann, T. 2000, Astrophys. J., 533, 682

Cantale, N., Courbin, F., Tewes, M., Jablonka, P., & Meylan, G. 2016, Astron. Astrophys., 589, A81

Cappellari, M. & Copin, Y. 2003, Mon. Not. R. Astron. Soc., 342, 345

Cerulo, P., Couch, W. J., Lidman, C., Demarco, R., Huertas-Company, M., Mei, S., Sánchez-Janssen, R., Barrientos, L. F., & Muñoz, R. 2017, Mon. Not. R. Astron. Soc., 472, 254

Chabrier, G. 2003, Publ. Astron. Soc. Pac., 115, 763

Chan, J. C. C., Beifiori, A., Mendel, J. T., Saglia, R. P., Bender, R., Fossati, M., Galametz, A., Wegner, M., Wilman, D. J., Cappellari, M., Davies, R. L., Houghton, R. C. W., Prichard, L. J., Lewis, I. J., Sharples, R., & Stott, J. P. 2016, Mon. Not. R. Astron. Soc., 458, 3181

Christlein, D. & Zabludoff, A. I. 2004, Astrophys. J., 616, 192

Cooper, M. C., Gallazzi, A., Newman, J. A., & Yan, R. 2010, Mon. Not. R. Astron. Soc., 402, 1942

Darvish, B., Mobasher, B., Sobral, D., Rettura, A., Scoville, N., Faisst, A., & Capak, P. 2016, Astrophys. J., 825, 113

Davis, M. & Geller, M. J. 1976, Astrophys. J., 208, 13

Dekel, A. & Silk, J. 1986, Astrophys. J., 303, 39

Dressler, A. 1980, Astrophys. J., 236, 351

Ellison, S. L., Patton, D. R., Mendel, J. T., & Scudder, J. M. 2011, Mon. Not. R. Astron. Soc., 418, 2043

Ellison, S. L., Patton, D. R., Simard, L., & McConnachie, A. W. 2008, Astron. J., 135, 1877

Elmegreen, D. M., Elmegreen, B. G., Ravindranath, S., & Coe, D. A. 2007, Astrophys. J., 658, 763

Ferrarese, L., Côté, P., Jordán, A., Peng, E. W., Blakeslee, J. P., Piatek, S., Mei, S., Merritt, D., Milosavljević, M., Tonry, J. L., & West, M. J. 2006, Astrophys. J. Suppl. Ser., 164, 334

Förster Schreiber, N. M., Shapley, A. E., Genzel, R., Bouché, N., Cresci, G., Davies, R., Erb, D. K., Genel, S., Lutz, D., Newman, S., Shapiro, K. L., Steidel, C. C., Sternberg, A., & Tacconi, L. J. 2011, Astrophys. J., 739, 45

Gehrels, N. 1986, Astrophys. J., 303, 336

Graves, G. J., Faber, S. M., & Schiavon, R. P. 2009, Astrophys. J., 693, 486

Gunn, J. E. & Gott, J. Richard, I. 1972, Astrophys. J., 176, 1

Guo, Y., Giavalisco, M., Cassata, P., Ferguson, H. C., Dickinson, M., Renzini, A., Koekemoer, A., Grogin, N. A., Papovich, C., Tundo, E., Fontana, A., Lotz, J. M., & Salimbeni, S. 2011, Astrophys. J., 735, 18

Hubble, E. P. 1926, Astrophys. J., 64, 321

Kauffmann, G., White, S. D. M., Heckman, T. M., Ménard, B., Brinchmann, J., Charlot, S., Tremonti, C., & Brinkmann, J. 2004, Mon. Not. R. Astron. Soc., 353, 713

Kawinwanichakij, L., Papovich, C., Quadri, R. F., Glazebrook, K., Kacprzak, G. G., Allen, R. J., Bell, E. F., Croton, D. J., Dekel, A., Ferguson, H. C., Forrest, B., Grogin, N. A., Guo, Y., Kocevski, D. D., Koekemoer, A. M., Labbé, I., Lucas, R. A., Nanayakkara, T., Spitler, L. R., Straatman, C. M. S., Tran, K.-V. H., Tomczak, A., & van Dokkum, P. 2017, Astrophys. J., 847, 134

Kissler-Patig, M., Pirard, J. F., Casali, M., Moorwood, A., Ageorges, N., Alves de Oliveira, C., Baksai, P., Bedin, L. R., Bendek, E., Biereichel, P., Delabre, B., Dorn, R., Esteves, R., Finger, G., Gojak, D., Huster, G., Jung, Y., Kiekebush, M., Klein, B., Koch, F., Lizon, J. L., Mehrgan, L., Petr-Gotzens, M., Pritchard, J., Selman, F., & Stegmeier, J. 2008, Astron. Astrophys., 491, 941

Kovač, K., Lilly, S. J., Knobel, C., Bschorr, T. J., Peng, Y., Carollo, C. M., Contini, T., Kneib, J. P., Le Févre, O., Mainieri, V., Renzini, A., Scodeggio, M., Zamorani, G., Bardelli, S., Bolzonella, M., Bongiorno, A., Caputi, K., Cucciati, O., de la Torre, S., de Ravel, L., Franzetti, P., Garilli, B., Iovino, A., Kampczyk, P., Lamareille, F., Le Borgne, J. F., Le Brun, V., Maier, C., Mignoli, M., Oesch, P., Pello, R., Montero, E. P., Presotto, V., Silverman, J., Tanaka, M., Tasca, L., Tresse, L., Vergani, D., Zucca, E., Aussel, H., Koekemoer, A. M., Le Floc'h, E., Moresco, M., & Pozzetti, L. 2014, Mon. Not. R. Astron. Soc., 438, 717

Kriek, M. & Conroy, C. 2013, Astrophys. J. Lett., 775, L16

Kriek, M., van Dokkum, P. G., Labbé, I., Franx, M., Illingworth, G. D., Marchesini, D., & Quadri, R. F. 2009, Astrophys. J., 700, 221

Kron, R. G. 1980, Astrophys. J. Suppl. Ser., 43, 305

Kroupa, P. 2001, Mon. Not. R. Astron. Soc., 322, 231

Lang, P., Wuyts, S., Somerville, R. S., Förster Schreiber, N. M., Genzel, R., Bell, E. F., Brammer, G., Dekel, A., Faber, S. r. M., Ferguson, H. C., Grogin, N. A., Kocevski, D. D., Koekemoer, A. M., Lutz, D., McGrath, E. J., Momcheva, I., Nelson, E. J., Primack, J. R., Rosario, D. J., Skelton, R. E., Tacconi, L. J., van Dokkum, P. G., & Whitaker, K. E. 2014, Astrophys. J., 788, 11

Larson, R. B., Tinsley, B. M., & Caldwell, C. N. 1980, Astrophys. J., 237, 692

Lidman, C., Suherli, J., Muzzin, A., Wilson, G., Demarco, R., Brough, S., Rettura, A., Cox, J., DeGroot, A., Yee, H. K. C., Gilbank, D., Hoekstra, H., Balogh, M., Ellingson, E., Hicks, A., Nantais, J., Noble, A., Lacy, M., Surace, J., & Webb, T. 2012, Mon. Not. R. Astron. Soc., 427, 550

Lin, Y.-T., Brodwin, M., Gonzalez, A. H., Bode, P., Eisenhardt, P. R. M., Stanford, S. A., & Vikhlinin, A. 2013, Astrophys. J., 771, 61

Lin, Y.-T., Hsieh, B.-C., Lin, S.-C., Oguri, M., Chen, K.-F., Tanaka, M., Chiu, I. N., Huang, S., Kodama, T., Leauthaud, A., More, S., Nishizawa, A. J., Bundy, K., Lin, L., & Miyazaki, S. 2017, Astrophys. J., 851, 139

Lotz, J. M., Koekemoer, A., Coe, D., Grogin, N., Capak, P., Mack, J., Anderson, J., Avila, R., Barker, E. A., & Borncamp, D. 2017, Astrophys. J., 837, 97

Lubin, L. M., Oke, J. B., & Postman, M. 2002, Astron. J., 124, 1905

Mannucci, F., Cresci, G., Maiolino, R., Marconi, A., & Gnerucci, A. 2010, Mon. Not. R. Astron. Soc., 408, 2115

Maraston, C. 2005, Mon. Not. R. Astron. Soc., 362, 799

Merritt, D. 1984, Astrophys. J., 276, 26

Moore, B., Katz, N., Lake, G., Dressler, A., & Oemler, A. 1996, Nature, 379, 613

Moster, B. P., Somerville, R. S., Maulbetsch, C., van den Bosch, F. C., Macciò, A. V., Naab, T., & Oser, L. 2010, Astrophys. J., 710, 903

Muzzin, A., Marchesini, D., van Dokkum, P. G., Labbé, I., Kriek, M., & Franx, M. 2009, Astrophys. J., 701, 1839

Muzzin, A., Wilson, G., Yee, H. K. C., Gilbank, D., Hoekstra, H., Demarco, R., Balogh, M., van Dokkum, P., Franx, M., Ellingson, E., Hicks, A., Nantais, J., Noble, A., Lacy, M., Lidman, C., Rettura, A., Surace, J., & Webb, T. 2012, Astrophys. J., 746, 188

Oemler, Augustus, J. 1974, Astrophys. J., 194, 1

Peng, C. Y., Ho, L. C., Impey, C. D., & Rix, H.-W. 2002, Astron. J., 124, 266

—. 2010, Astron. J., 139, 2097

Pintos-Castro, I., Yee, H. K. C., Muzzin, A., Old, L., & Wilson, G. 2019, Astrophys. J., 876, 40

Postman, M., Coe, D., Benítez, N., Bradley, L., Broadhurst, T., Donahue, M., Ford, H., Graur, O., Graves, G., & Jouvel, S. 2012, Astrophys. J. Suppl. Ser., 199, 25

Postman, M., Franx, M., Cross, N. J. G., Holden, B., Ford, H. C., Illingworth, G. D., Goto, T., Demarco, R., Rosati, P., Blakeslee, J. P., Tran, K. V., Benítez, N., Clampin, M., Hartig, G. F., Homeier, N., Ardila, D. R., Bartko, F., Bouwens, R. J., Bradley, L. D., Broadhurst, T. J., Brown, R. A., Burrows, C. J., Cheng, E. S., Feldman, P. D., Golimowski, D. A., Gronwall, C., Infante, L., Kimble, R. A., Krist, J. E., Lesser, M. P., Martel, A. R., Mei, S., Menanteau, F., Meurer, G. R., Miley, G. K., Motta, V., Sirianni, M., Sparks, W. B., Tran, H. D., Tsvetanov, Z. I., White, R. L., & Zheng, W. 2005, Astrophys. J., 623, 721

Postman, M. & Geller, M. J. 1984, Astrophys. J., 281, 95

Quadri, R. F., Williams, R. J., Franx, M., & Hildebrandt, H. 2012, Astrophys. J., 744, 88

Salim, S., Rich, R. M., Charlot, S., Brinchmann, J., Johnson, B. D., Schiminovich, D., Seibert, M., Mallery, R., Heckman, T. M., Forster, K., Friedman, P. G., Martin, D. C., Morrissey, P., Neff, S. G., Small, T., Wyder, T. K., Bianchi, L., Donas, J., Lee, Y.-W., Madore, B. F., Milliard, B., Szalay, A. S., Welsh, B. Y., & Yi, S. K. 2007, Astrophys. J. Suppl. Ser., 173, 267

Salpeter, E. E. 1955, Astrophys. J., 121, 161

Shipley, H. V., Lange-Vagle, D., Marchesini, D., Brammer, G. B., Ferrarese, L., Stefanon, M., Kado-Fong, E., Whitaker, K. E., Oesch, P. A., Feinstein, A. D., Labbé, I., Lundgren, B., Martis, N., Muzzin, A., Nedkova, K., Skelton, R., & van der Wel, A. 2018, Astrophys. J. Suppl. Ser., 235, 14

Smith, R. J., Hudson, M. J., Lucey, J. R., Nelan, J. E., & Wegner, G. A. 2006, Mon. Not. R. Astron. Soc., 369, 1419

Sorba, R. & Sawicki, M. 2015, Mon. Not. R. Astron. Soc., 452, 235

Stott, J. P., Sobral, D., Swinbank, A. M., Smail, I., Bower, R., Best, P. N., Sharples, R. M., Geach, J. E., & Matthee, J. 2014, Mon. Not. R. Astron. Soc., 443, 2695

Suess, K. A., Kriek, M., Price, S. H., & Barro, G. 2019, Astrophys. J., 877, 103

Szomoru, D., Franx, M., van Dokkum, P. G., Trenti, M., Illingworth, G. D., Labbé, I., & Oesch, P. 2013, Astrophys. J., 763, 73

van den Bosch, F. C., Aquino, D., Yang, X., Mo, H. J., Pasquali, A., McIntosh, D. H., Weinmann, S. M., & Kang, X. 2008, Mon. Not. R. Astron. Soc., 387, 79

van der Wel, A., Franx, M., van Dokkum, P. G., Skelton, R. E., Momcheva, I. G., Whitaker, K. E., Brammer, G. B., Bell, E. F., Rix, H. W., Wuyts, S., Ferguson, H. C., Holden, B. P., Barro, G., Koekemoer, A. M., Chang, Y.-Y., McGrath, E. J., Häussler, B., Dekel, A., Behroozi, P., Fumagalli, M., Leja, J., Lundgren, B. F., Maseda, M. V., Nelson, E. J., Wake, D. A., Patel, S. G., Labbé, I., Faber, S. M., Grogin, N. A., & Kocevski, D. D. 2014, Astrophys. J., 788, 28

van Dokkum, P. G., Franx, M., Fabricant, D., Illingworth, G. D., & Kelson, D. D. 2000, Astrophys. J., 541, 95

Veilleux, S., Cecil, G., & Bland-Hawthorn, J. 2005, Annu. Rev. Astron. Astrophys., 43, 769

Wetzel, A. R., Tinker, J. L., & Conroy, C. 2012, Mon. Not. R. Astron. Soc., 424, 232

Wuyts, S., Cox, T. J., Hayward, C. C., Franx, M., Hernquist, L., Hopkins, P. F., Jonsson, P., & van Dokkum, P. G. 2010, Astrophys. J., 722, 1666

Wuyts, S., Förster Schreiber, N. M., Genzel, R., Guo, Y., & Barro, G. o. 2012, Astrophys. J., 753, 114

York, D. G., Adelman, J., Anderson, John E., J., Anderson, S. F., Annis, J., Bahcall, N. A., Bakken, J. A., Barkhouser, R., Bastian, S., Berman, E., Boroski, W. N., Bracker, S., Briegel, C., Briggs, J. W., Brinkmann, J., Brunner, R., Burles, S., Carey, L., Carr, M. A., Castander, F. J., Chen, B., Colestock, P. L., Connolly,

A. J., Crocker, J. H., Csabai, I., Czarapata, P. C., Davis, J. E., Doi, M., Dombeck, T., Eisenstein, D., Ellman, N., Elms, B. R., Evans, M. L., Fan, X., Federwitz, G. R., Fiscelli, L., Friedman, S., Frieman, J. A., Fukugita, M., Gillespie, B., Gunn, J. E., Gurbani, V. K., de Haas, E., Haldeman, M., Harris, F. H., Hayes, J., Heckman, T. M., Hennessy, G. S., Hindsley, R. B., Holm, S., Holmgren, D. J., Huang, C.-h., Hull, C., Husby, D., Ichikawa, S.-I., Ichikawa, T., Ivezić, Ž., Kent, S., Kim, R. S. J., Kinney, E., Klaene, M., Kleinman, A. N., Kleinman, S., Knapp, G. R., Korienek, J., Kron, R. G., Kunszt, P. Z., Lamb, D. Q., Lee, B., Leger, R. F., Limmongkol, S., Lindenmeyer, C., Long, D. C., Loomis, C., Loveday, J., Lucinio, R., Lupton, R. H., MacKinnon, B., Mannery, E. J., Mantsch, P. M., Margon, B., McGehee, P., McKay, T. A., Meiksin, A., Merelli, A., Monet, D. G., Munn, J. A., Narayanan, V. K., Nash, T., Neilsen, E., Neswold, R., Newberg, H. J., Nichol, R. C., Nicinski, T., Nonino, M., Okada, N., Okamura, S., Ostriker, J. P., Owen, R., Pauls, A. G., Peoples, J., Peterson, R. L., Petravick, D., Pier, J. R., Pope, A., Pordes, R., Prosapio, A., Rechenmacher, R., Quinn, T. R., Richards, G. T., Richmond, M. W., Rivetta, C. H., Rockosi, C. M., Ruthmansdorfer, K., Sand ford, D., Schlegel, D. J., Schneider, D. P., Sekiguchi, M., Sergey, G., Shimasaku, K., Siegmund, W. A., Smee, S., Smith, J. A., Snedden, S., Stone, R., Stoughton, C., Strauss, M. A., Stubbs, C., SubbaRao, M., Szalay, A. S., Szapudi, I., Szokoly, G. P., Thakar, A. R., Tremonti, C., Tucker, D. L., Uomoto, A., Vanden Berk, D., Vogeley, M. S., Waddell, P., Wang, S.-i., Watanabe, M., Weinberg, D. H., Yanny, B., Yasuda, N., & SDSS Collaboration. 2000, Astron. J., 120, 1579

Zolotov, A., Dekel, A., Mandelker, N., Tweed, D., Inoue, S., DeGraf, C., Ceverino, D., Primack, J. R., Barro, G., & Faber, S. M. 2015, Mon. Not. R. Astron. Soc., 450, 2327